The American Journal of Pathology, Vol. 189, No. 3, March 2019

ELSEVIER

The American Journal of
PATHOLOGY
ajp.amjpathol.org

ANIMAL MODELS

Spatiotemporally Skewed Activation of Programmed Cell Death Receptor 1—Positive T Cells after Epstein-Barr Virus Infection and Tumor Development in Long-Term Fully Humanized Mice

Simon Danisch,[*†] Constanze Slabik,[*†] Angela Cornelius,[*†] Manuel Albanese,[‡] Takanobu Tagawa,[‡] Yen-Fu A. Chen,[‡] Nicole Krönke,[§] Britta Eiz-Vesper,[¶] Stefan Lienenklaus,[‖] Andre Bleich,[‖] Sebastian J. Theobald,[*†] Andreas Schneider,[*†] Arnold Ganser,[*] Constantin von Kaisenberg,[**] Reinhard Zeidler,[‡††] Wolfgang Hammerschmidt,[‡] Friedrich Feuerhake,[§‡‡] and Renata Stripecke[*†]

From the Departments of Hematology, Hemostasis, Oncology and Stem Cell Transplantation and Obstetrics, Gynecology and Reproductive Medicine,** the Institute of Pathology,[§] and the Institutes for Transfusion Medicine[¶] and Laboratory Animal Science,[‖] Hannover Medical School, Hannover; the Laboratory of Regenerative Immune Therapies Applied,[†] Excellence Cluster REBIRTH and German Centre for Infection Research, Partner Site Hannover, Hannover; the Research Unit Gene Vectors,[‡] Helmholtz Zentrum München, German Research Center for Environmental Health and German Centre for Infection Research, Partner Site Munich, Munich; the Department of Otorhinolaryngology,[††] Klinikum der Universität and German Centre for Infection Research, Partner Site Munich, Munich; and the Institute for Neuropathology,[‡‡] University Clinic Freiburg, Freiburg, Germany*

Accepted for publication November 6, 2018.

Address correspondence to Renata Stripecke, Dr.rer.nat.hab. Hannover Medical School, Carl-Neuberg Str 1, K11/HBZ Room 6100, 30625 Hannover, Germanystripecke. E-mail: renata@mh-hannover.de.

Humanized mice developing functional human T cells endogenously and capable of recognizing cognate human leukocyte antigen—matched tumors are emerging as relevant models for studying human immuno-oncology *in vivo*. Herein, mice transplanted with human $CD34^+$ stem cells and bearing endogenously developed human T cells for >15 weeks were infected with an oncogenic recombinant Epstein-Barr virus (EBV), encoding enhanced firefly luciferase and green fluorescent protein. EBV—firefly luciferase was detectable 1 week after infection by noninvasive optical imaging in the spleen, from where it spread rapidly and systemically. EBV infection resulted into a pronounced immunologic skewing regarding the expansion of $CD8^+$ T cells in the blood outnumbering the $CD4^+$ T and $CD19^+$ B cells. Furthermore, within 10 weeks of infections, mice developing EBV-induced tumors had significantly higher absolute numbers of $CD8^+$ T cells in lymphatic tissues than mice controlling tumor development. Tumor outgrowth was paralleled by an up-regulation of the programmed cell death receptor 1 on $CD8^+$ and $CD4^+$ T cells, indicative for T-cell dysfunction. Histopathological examinations and *in situ* hybridizations for EBV in tumors, spleen, liver, and kidney revealed foci of EBV-infected cells in perivascular regions in close association with programmed cell death receptor 1—positive infiltrating lymphocytes. The strong spatiotemporal correlation between tumor development and the T-cell dysfunctional status seen in this viral oncogenesis humanized model replicates observations obtained in the clinical setting. *(Am J Pathol 2019, 189: 521—539; https://doi.org/10.1016/j.ajpath.2018.11.014)*

Supported by German Center for Infection Research grant DZIF TTU07.803 (R.S., R.Z. and W.H.), German Research Council grant DFG/SFB738 Project A6 (R.S.), German Research Council DFG/REBIRTH Unit 6.4 (R.S.), German Research Council SFB1064/TP A04 and TP A13, SFB-TR36/TP A04, German Cancer Aid grants 107277 (W.H.) and 109661 (W.H.), National Cancer Institute grant CA70723, German Exchange Service personal grant (T.T.), German Federal Ministry of Education and Research grants, Sponsor Jülich grant 031B0006C (ILUMINATE), and Sponsor DLR grant 01ZX1608A (SYSIMIT) (F.F.), and a RegSci Ph.D. fellowship (S.J.T.).

S.D. and C.S. contributed equally to this work.

W.H., F.F., and R.S. contributed equally as senior authors.

Disclosures: R.S. received honoraria as a lecturer in conferences from The Jackson Laboratory, which commercially distributes the nonobese diabetic $Rag1^{null}$ $IL2rg^{null}$ mice.

https://doi.org/10.1016/j.ajpath.2018.11.014

In recent years, immunotherapeutic approaches with immune checkpoint inhibitors showed unprecedented and long-lasting responses even in cancer patients with advanced disease.[1] Nivolumab, an antibody blocking the programmed cell death receptor (PD)-1, inhibited tumor immune evasion in patients with relapsed or refractory Hodgkin lymphoma (HL) with remarkable 87% objective responses.[2] Consequently, a promising rich pipeline of novel therapeutic antibodies and innovative combination therapies targeting checkpoint molecules expressed on T cells and/or tumor cells is currently being developed to abrogate tumor-induced immunosuppression. A limitation in this preclinical field is testing these human-specific antibodies *in vivo* because the immune responses obtained in mice or nonhuman primates sometimes do not predict what can be observed in immunologically distinct and genetically heterogeneous humans. Therefore, novel *in vivo* models suitable for validating these immunotherapies are warranted to accelerate their translation to patients. Mice reconstituted with a human immune system (alias humanized mice) have emerged in the past decade as an important preclinical platform for *in vivo* efficacy testing of human-specific therapeutic drugs.[3] Several groups have reported that the use of $CD34^+$ human hematopoietic stem cell transplantation (huHSCT) into severely immune-deficient mouse strains, such as nonobese diabetic (NOD)/severe combined immune-deficient $IL2rg^{null}$,[4] NOD $Rag1^{null}$ $IL2rg^{null}$,[5,6] or BALB/c-$Rag2^{null}$ $Il2rg^{null}$[7] mice, resulted in consistent human hematopoietic engraftment in the bone marrow and development of human lymphocytes in lymphatic tissues. Remarkably, highly xenoreactive human T cells seem to be functionally depleted in the thymus, so that endogenously developing human mature T cells can persist long-term for several months up to nearly a year after huHSCT with only sporadic occurrence of graft-*versus*-host disease.[6,8] Concurrently, patient-derived tumor xenograft cancer models transplanted into NOD/severe combined immune-deficient $IL2rg^{null}$ mice showed that these *in vivo* models can be predictive of clinical outcomes.[9] Patient-derived tumor xenograft mouse models combined with humanized immune systems could further enable their use for testing immunotherapies. Recently, Wang et al[10] showed that after huHSCT, NOD/severe combined immune-deficient $IL2rg^{null}$ humanized mice transplanted with patient-derived tumor xenograft cells matched to a few but not all of the class I human leukocyte antigen developed tumors. Moreover, treatment with an anti−PD-1 antibody (pembrolizumab) showed significant tumor growth inhibition. Inherent limitations of patient-derived tumor xenograft models surgically grafted into humanized mice include human leukocyte antigen mismatch between stem cell donor(s) and tumors and sequential loss of the original tumor microenvironment (TME) during tumor outgrowth in the mouse. Both problems can be overcome in an *in vivo* model of virus-induced hematological tumors, in which the malignant cells and the immune system carry the same human leukocyte antigens and tissue antigens and the neoplasm development induces its own individual TME. Epstein-Barr virus (EBV) is a type 1 carcinogen that is directly associated with the development of human B-cell neoplasms.[11] EBV infection models in humanized mice 6 to 10 weeks after huHSCT have been described previously.[12−14] Nevertheless, at this early time point, the human immune reconstitution consists of an insufficient development, maturation, and egress of human lymphocytes from primary lymphatic tissues to the periphery, and it is thus not advanced enough to counteract the virus and explosive outgrowth of EBV-induced tumors.[15−18] Indeed, one study by Lee et al[19] elegantly showed that the time point of EBV infection after huHSCT critically affected the burden and types of developing tumors. Thus, consistent outgrowth of tumors resembling non-Hodgkin lymphomas developed when EBV infection occurred at 8 weeks after huHSCT (when immature B cells predominated, and T cells were lacking), whereas fewer tumors developed and resembled the TME of HL when mice were infected 15 weeks after huHSCT (at the time point when T-cell development and maturation can be observed in this model). These HL-like tumors were histologically more complex and contained Hodgkin Reed-Sternberg−like cells.[19] These observations by Lee et al[19] suggested a link between the level of reconstitution of the human adaptive immunity in humanized mice and the shaping of the tumor and, in turn, the establishment of an immunosuppressive TME. Herein, we hypothesized that EBV infection and tumor progression in long-term humanized mice would shape the activation of T-cell lineages and induce PD-1 up-regulation. The data reveal that most mice infected with EBV 15 to 17 weeks after huHSCT and analyzed 10 weeks later did not develop macroscopically detectable tumors, but nevertheless showed a skewed $CD8^+$ T-cell expansion in several lymphatic tissues compared with noninfected mice. In animals showing tumors caused by EBV infection, an even more substantial expansion of $CD8^+$ $PD\text{-}1^+$ T cells was observed in tumor tissues. Histopathology analyses of adjacent tissue, combined with EBER *in situ* hybridization, characteristically revealed recurrent patterns of spatial organization with foci of EBV-infected cells in close association with $PD\text{-}1^+$ infiltrating lymphocytes, often in perivascular regions. Therefore, long-term humanized mice infected with EBV demonstrated a range of dynamic and vigorous interplay between tumor development and the immune system in multiple organs. This working model recapitulates clinical findings of chronic and acute EBV infection and could be used to study systemic T-cell activation and local responses in the TME at different stages of organ involvement and tumor formation.

Materials and Methods

Ethics Statement

All subjects donating cord blood provided written informed consent. This study was approved by the Ethics Committee of Hannover Medical School (Hannover, Germany).

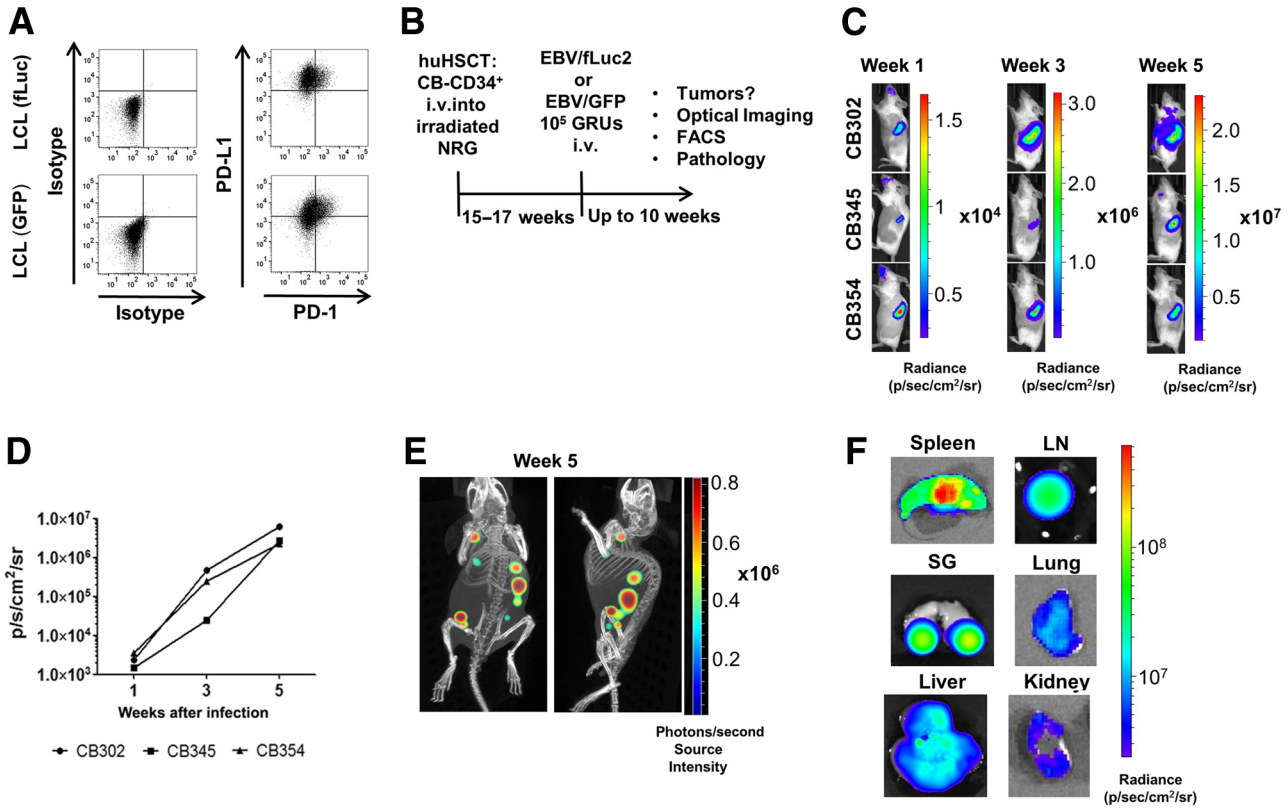

Figure 1 Epstein-Barr virus (EBV) infection intravenously primarily targets the spleen and spreads systemically. **A:** Flow cytometry analyses of PD-L1 and PD-1 expression on lymphoblastoid cell lines (LCLs) generated using EBV/B95.8-green fluorescent protein (GFP) or EBV/B95.8—firefly luciferase (fLuc2). **B:** A schematic representation of experiments. Humanized mice were infected with 10^5 GFP Raji infectious units (GRUs) of either EBV/B95.8-GFP or EBV/B95.8-fLuc2 15 weeks after huHSCT. Mice infected with EBV/B95.8-fLuc2 were longitudinally monitored for biodistribution of EBV infection by optical imaging and computed tomographic analyses, and mice infected with EBV/B95.8-GFP were regularly bled to monitor the dynamics of reconstitution of human lymphocytes. For both experimental setups, mice were euthanized 10 weeks after infection. **C:** Luciferase signal of three representative EBV/B95.8/fLuc2 infected humanized mice generated with stem cells from different cord blood (CB) is displayed in a two-dimensional bioluminescence analysis in lateral view at weeks 1, 3, and 5 after infection. **D:** Quantification of the intensity of bioluminescence in the spleen region over the course of the experiment. **E:** Three-dimensional analysis 5 weeks after infection using IVIS SpectrumCT and LivingImage. **F:** *Ex vivo* optical imaging analysis of explanted tissues showing bioluminescence signals. FACS, fluorescence-activated cell sorting; LN, lymph node; NRG, nonobese diabetic *Rag1*^{null} *IL2rg*^{null}; p/s/cm^2/sr, average radiance; PD-L1, programmed cell death ligand 1; SG, salivary glands.

Generation of EBV Engineered Strains

EBV-B95.8/green fluorescent protein (GFP) is a genetically modified strain (alias 2089-EBV), derived from the B95-8 strain,[20,21] and was amplified in HEK293 cells, as described.[22] EBV-B95.8/firefly luciferase 2 (fLuc2) was derived from the EBV-B95.8/GFP strain and contains a codon-optimized fLuc cDNA (*luc2*; Genscript Biotech, Piscataway Township, NJ) coupled to a preceding T2A element and engineered to be expressed downstream of the viral Epstein-Barr nuclear antigen 2 (*EBNA2*) gene. The viral genome was constructed using recombinant DNA technologies in a modified *Escherichia coli* DH10B strain.[23–25] The resulting maxi-EBV plasmid p6476 was carefully analyzed by restriction enzyme analysis, and all relevant genetically modified regions were confirmed by sequencing. The EBV-B95.8/fLuc2 virus was introduced into HEK293 cells, and single-cell clones were isolated and induced to produce progeny virus. Viral titers were determined and indicated as GFP Raji infectious units, as previously described.[26]

Generation of Humanized Mice

All experiments involving mice were performed in accordance with the regulations and guidelines of the animal welfare of the State of Lower Saxony (Niedersächsisches Landesamt für Verbraucherschutz und Lebensmittelsicherheit, Dezernat 33/Tierschutz). NOD *Rag1*^{null} *IL2rg*^{null} mice, aged 4 to 6 weeks, were originally obtained from The Jackson Laboratory (Bar Harbor, ME) and bred in house under pathogen-free conditions. Cord blood (CB) units were obtained after informed consent from donors (mothers at term), and study protocols were approved by the Ethics Committee of the Hannover Medical School. Human CD34$^+$ hematopoietic cells were isolated from CB after two rounds of positive selection using immune magnetic beads (Direct CD34 Progenitor Cell Isolation Kit, human; MACS Miltenyi Biotec, Bergisch Gladbach, Germany), as described.[27] CD34$^+$/CB units were pretested in a couple of transplanted mice, and only those resulting into 20% or higher frequencies of human CD45$^+$ cells in mouse peripheral blood lymphocytes 15 weeks after HSCT were used

Table 1 Mouse Characteristics

Mouse ID	Sex	Cord blood ID	Group	hHSCT ID	CD45 %	EBV detection (qPCR/EBER FISH)	Tumors
601	M	263	Control	88	23.7	−/ND	Liver (mouse)
Z6	F	215	Control	95	68	−/ND	No
Z5	F	215	Control	95	41.7	−/ND	No
Z4	F	215	Control	95	55.8	−/ND	No
Z17	F	185	Control	96	42.7	−/ND	No
Z10	F	185	Control	96	47.5	−/ND	No
1481	F	272	Control	105	82	−/ND	No
1480	F	272	Control	105	75.3	−/ND	No
1062	F	229	Control	92	58.2	−/ND	No
1061	F	229	Control	92	33.5	−/ND	No
1060	F	229	Control	92	21.7	−/ND	No
618	M	195	Control	88	70.5	−/ND	No
616	M	153	Control	88	84.8	−/ND	No
603	F	212	Control	89	83.8	−/ND	No
600	F	212	Control	89	81.6	−/ND	No
582	M	264	Control	88	65.6	−/ND	No
188	F	230	Control	83	72.5	−/ND	No
12	F	222	Control	108	22.1	−/ND	No
2	F	222	Control	109	44.6	−/ND	No
1508	F	272	EBV	105	75	−/+	No
1469	F	147	EBV	104	61.7	+/ND	No
1391	F	147	EBV	104	66.2	+/ND	No
1016	F	229	EBV	92	16.1	+/ND	No
1014	F	229	EBV	92	25.7	+/+	No
617	M	195	EBV	88	72.9	+/+	No
615	M	153	EBV	88	72	+/+	No
606	F	212	EBV	89	82.7	−/+	No
605	F	212	EBV	89	76.9	+/ND	No
604	F	212	EBV	89	83.9	−/+	No
599	M	264	EBV	88	60.7	+/ND	No
1509	F	272	EBV-Tumor	105	83.8	−/+	SPL
1440	F	147	EBV-Tumor	104	49.3	+/+	SPL
3	F	222	EBV-Tumor	109	72.5	+/ND	SPL
1510	F	272	EBV-Tumor	105	79.4	+/+	SPL
602	M	263	EBV-Tumor	88	15.5	+/ND	SPL, KID, PA
1570	F	222	EBV-Tumor	108	77.7	+/ND	SPL, LIV
187	F	230	EBV-Tumor	83	50.9	+/+	SPL, LIV
1015	F	229	EBV-Tumor	92	50	+/+	SPL, KID, LIV

F, female; M, male; +, positive; −, negative; EBV, Epstein-Barr virus; FISH, *in situ* hybridization; ID, identification; KID, kidney; LIV, liver; ND, not determined; PA, pancreas; qPCR, real-time quantitative PCR; SPL, spleen.

for further experiments. Before HSCT, mice were sublethally irradiated (450 cGy) using a [^{137}Cs] column irradiator (Gammacell 3000 Elan; Best Theratronics, Ottawa, ON, Canada). At 4 hours after irradiation, 2.0×10^5 CD34$^+$ cells were administrated to mice through the tail vein, as described.[6,28] For these experiments, both male and female mice were used.

Analysis of Human T- and B-Cell Reconstitution in Different Tissues

Patterns of human T- and B-cell reconstitution in peripheral blood, spleen, mesenteric lymph nodes (mLNs), peripheral lymph nodes (LNs), and bone marrow (BM) were analyzed by flow cytometry, essentially as described,[6,28] with minor modifications. Lysis of erythrocytes was performed in 0.83% ammonium chloride/20 mmol/L HEPES, pH 7.2, for 5 minutes at room temperature, followed by stabilization with cold phosphate-buffered saline (Biochrom, Berlin, Germany) and washing. Spleen, peripheral LNs, mLNs, and BM cells were isolated and homogenized. Before homogenization, the spleen was cut in small pieces and predigested with 2 mg/mL Collagenase D (Roche, Mannheim, Germany) and 2 U/mL DNAseI (NEB, Frankfurt, Germany) in RPMI 1640 medium (Thermo Fisher Scientific, Waltham, MA) at

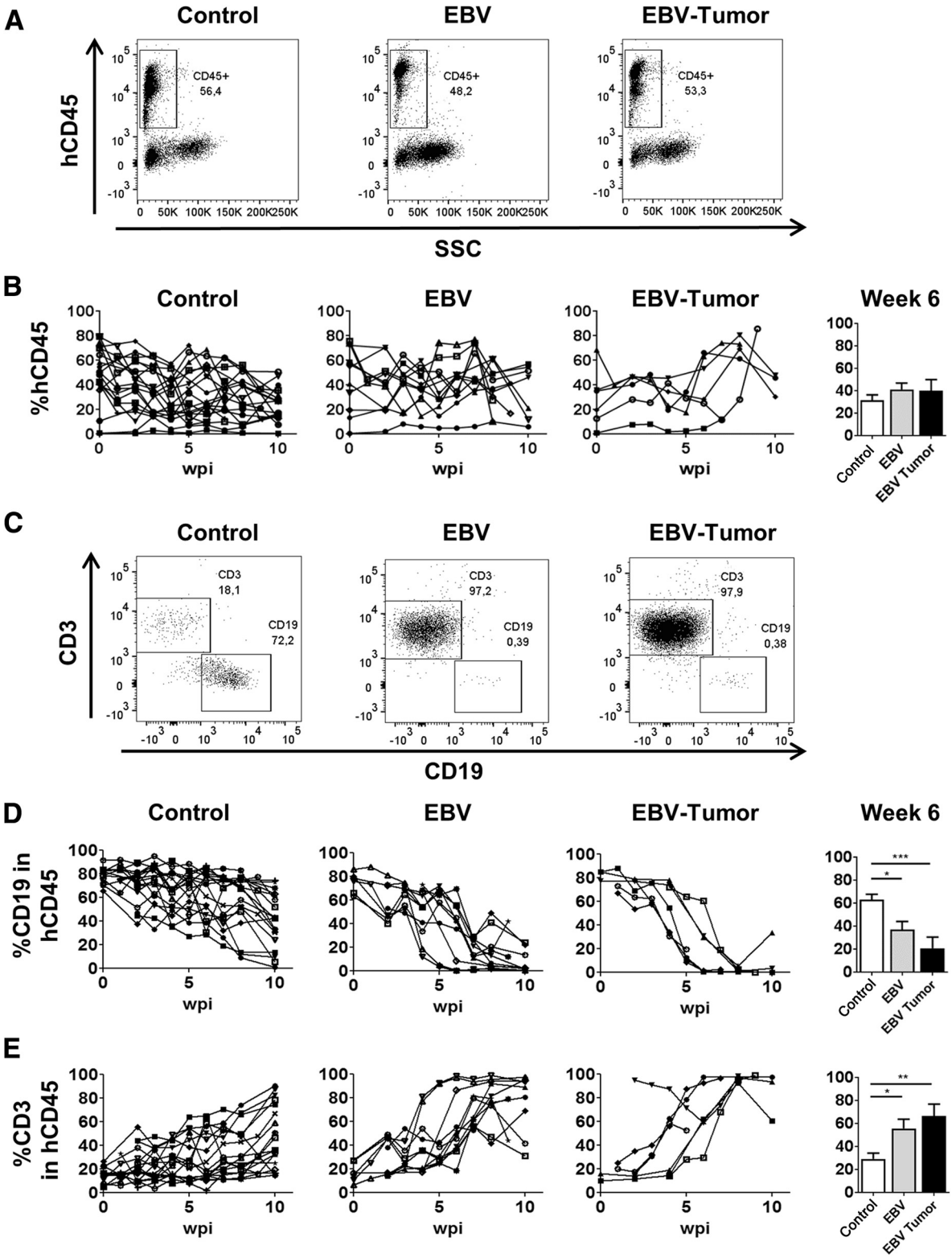

Figure 2 Dynamics of frequencies of human CD45$^+$ (hCD45$^+$) in peripheral blood and relative frequencies of CD19$^+$ and CD3$^+$ lymphocytes within hCD45 cells. Results are shown for control, Epstein-Barr virus (EBV), and EBV-Tumor cohorts, and the bar graphs represent the data analyzed on week 6 after infection. Bars filled with white, gray, and black represent control, EBV, and EBV-Tumor cohorts, respectively. **A** and **B:** Examples displayed for control, EBV, and EBV-Tumor representative mice 6 weeks after infection, showing the gating strategy for the CD45$^+$ population (**A**) and overall results and a bar graph each showing mean and SEM of each group 6 weeks after infection (**B**). **C:** Exemplary results for CD19$^+$ and CD3$^+$ populations (gated in CD45$^+$). **D** and **E:** CD19 (**D**) and CD3 (**E**) (gated in CD45$^+$) over the course of the experiment, and a bar graph each showing SEM of each group 6 weeks after infection. Six weeks after infection was chosen as a time point for statistical analyses because it best signaled the turning point of the dynamics in the lymphocyte population. $^*P < 0.05$, $^{**}P < 0.01$, and $^{***}P < 0.001$. K, 1000; SSC, side scatter; wpi, weeks post infection.

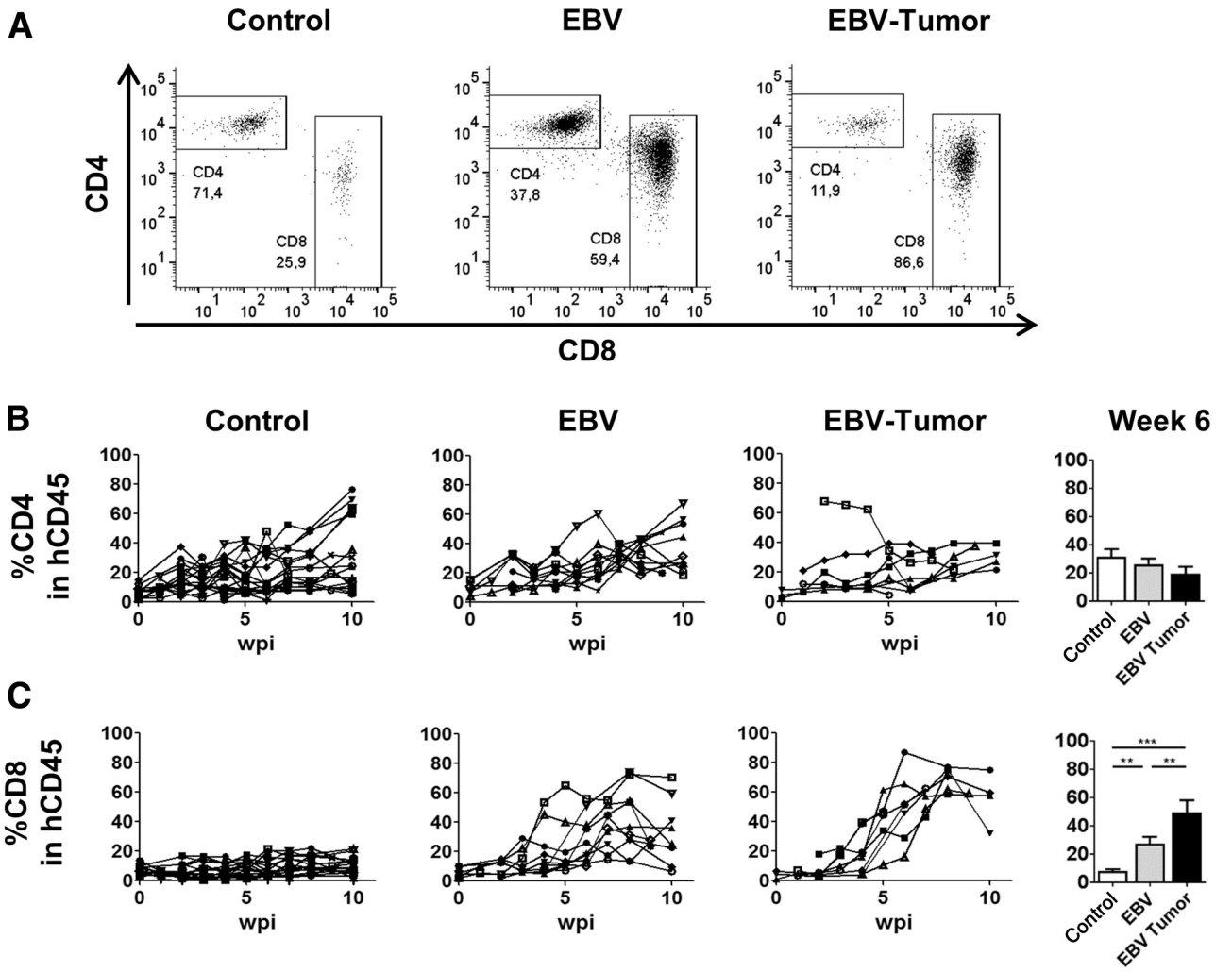

Figure 3 Dynamics of relative frequencies of human $CD4^+$ and $CD8^+$ lymphocytes in human $CD45^+$ ($hCD45^+$) cells of peripheral blood. Results are shown for control, Epstein-Barr virus (EBV), and EBV-Tumor cohorts, and the bar graphs represent the data analyzed on week 6 after infection. Bars filled with white, gray, and black represent control, EBV, and EBV-Tumor cohorts, respectively. **A:** Examples displayed for control, EBV, and EBV-Tumor representative mice 6 weeks after infection, showing the $CD4^+$ and $CD8^+$ populations (gated in $CD45^+$ $CD3^+$ T cells). **B** and **C:** CD4 (**B**) and CD8 (**C**) frequencies relative to human $CD45^+$ cells detected in mice over the course of the experiment and a bar graph, each showing SEM of each group 6 weeks after infection. $^{**}P < 0.01$, $^{***}P < 0.001$. wpi, weeks post infection.

37°C for 1 to 2 hours. Cell suspensions were washed and resuspended in phosphate-buffered saline for counting and staining with the following fluorochrome-conjugated monoclonal antibodies: Pacific blue anti-CD45, Alexa Flour 700 anti-CD19, brilliant violet 510 anti-CD3, peridinin chlorophyll anti-CD4, phycoerythrin-cyanine 7 anti-CD8, phycoerythrin anti−PD-1, allophycocyanin anti-CD69, allophycocyanin anti-CD366 [T-cell

Table 2 Quantified Absolute Cell Numbers Obtained for Spleen ($CD45^+$, $CD3^+$, $CD19^+$, $CD8^+$, $CD4^+$, $CD8^+$/$PD\text{-}1^+$, $CD4^+$/$PD\text{-}1^+$) and EBV DNA Copies Detected in Spleen

Variable	Control ($n = 17$)	EBV ($n = 11$)	EBV-Tumor ($n = 6$)
CD45	$8.615 \times 10^6 \pm 1.53 \times 10^7$	$9.485 \times 10^6 \pm 6.458 \times 10^6$	$2.022 \times 10^7 \pm 1.469 \times 10^7$
CD3	$2.994 \times 10^6 \pm 5.729 \times 10^6$	$6.759 \times 10^6 \pm 4.317 \times 10^6$	$1.805 \times 10^7 \pm 1.380 \times 10^7$
CD19	$4.994 \times 10^6 \pm 8.846 \times 10^6$	$2.141 \times 10^6 \pm 2.767 \times 10^6$	$1.347 \times 10^6 \pm 1.67 \times 10^6$
CD8	$9.549 \times 10^5 \pm 1.996 \times 10^6$	$3.415 \times 10^6 \pm 2.049 \times 10^6$	$1.132 \times 10^7 \pm 8.366 \times 10^6$
CD4	$1.973 \times 10^6 \pm 3.775 \times 10^6$	$3.056 \times 10^6 \pm 2.456 \times 10^6$	$6.191 \times 10^6 \pm 5.861 \times 10^6$
$CD8^+$ $PD\text{-}1^+$	$9.719 \times 10^5 \pm 2.119 \times 10^6$	$3.055 \times 10^6 \pm 1.985 \times 10^6$	$8.941 \times 10^6 \pm 4.562 \times 10^6$
$CD4^+$ $PD\text{-}1^+$	$1.772 \times 10^6 \pm 3.407 \times 10^6$	$2.691 \times 10^6 \pm 2.21 \times 10^6$	$5.384 \times 10^6 \pm 4.528 \times 10^6$
Copies/μg DNA	0 ± 0	$9.420 \times 10^2 \pm 1.88 \times 10^3$	$1.680 \times 10^4 \pm 2.7 \times 10^4$

Data are expressed as means ± SD.
EBV, Epstein-Barr virus.

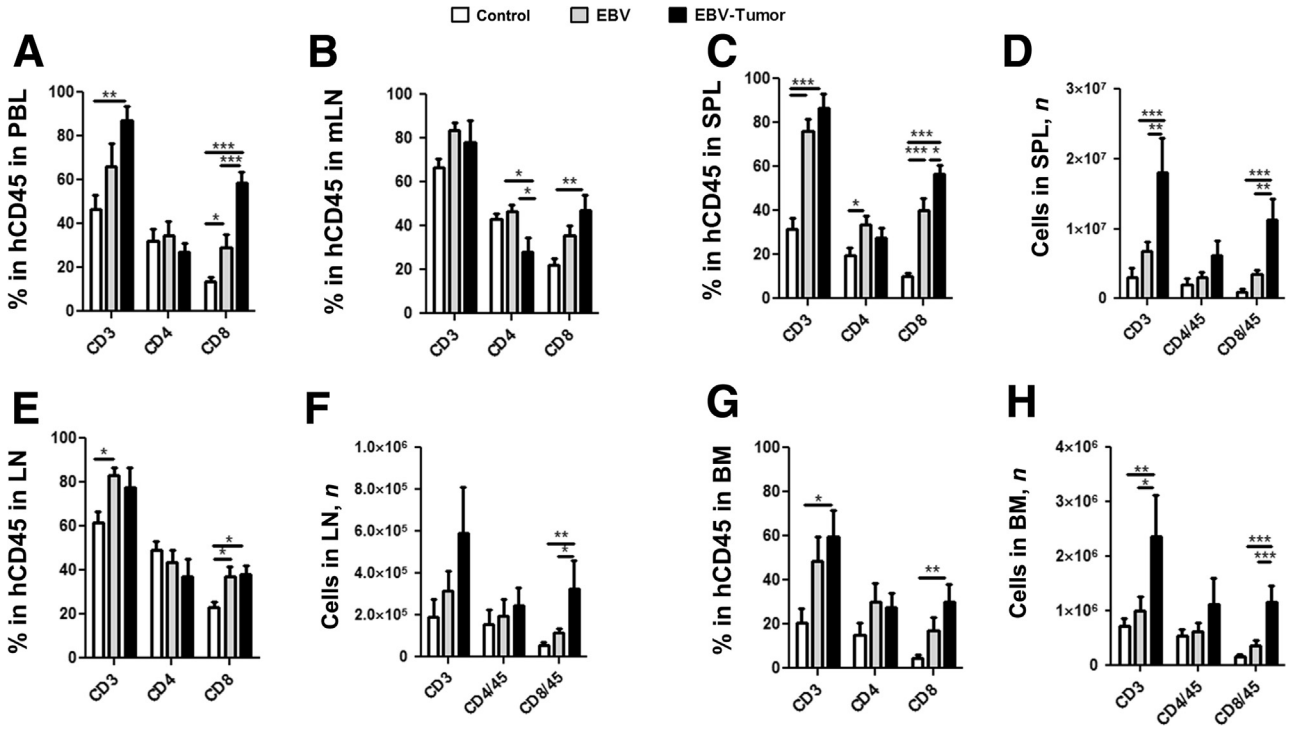

Figure 4 End point analyses of the frequencies and absolute counts of human T lymphocytes in different tissues. Bars filled with white, gray, and black represent control, Epstein-Barr virus (EBV), and EBV-Tumor cohorts, respectively. **A:** Frequencies of CD3$^+$, CD4$^+$, and CD8$^+$ in CD45$^+$ cells in peripheral blood are shown for control, EBV, and EBV-Tumor groups. **B:** Mesenteric lymph nodes were analyzed, as previously mentioned (*Materials and Methods*), for control, EBV, and EBV-Tumor groups. Splenocytes were recovered from mice, counted, stained, and analyzed, as mentioned above. **C** and **D:** Frequencies are depicted (**C**) and absolute numbers (**D**) for control, EBV, and EBV-Tumor animals. **E** and **F:** CD3$^+$, CD4$^+$, and CD8$^+$ frequencies in lymph nodes (**E**) and absolute cell numbers (**F**) for control, EBV, and EBV-Tumor groups. **G** and **H:** Frequencies (**G**) and absolute cell numbers (**H**) in bone marrow in control, EBV, and EBV-Tumor groups. $n = 19$ (**A**, **C**, **D**, **G**, and **H**, control group); $n = 11$ (**A** and **C**—**H**, EBV group, and **B**, control group); $n = 8$ (**A** and **C**—**H**, EBV-Tumor group, and **B**, EBV group); $n = 7$ (**B**, EBV-Tumor group); $n = 18$ (**E** and **F**, control group). $^*P < 0.05$, $^{**}P < 0.01$, and $^{***}P < 0.001$. BM, bone marrow; hCD45, human CD45; LN, lymph node; mLN, mesenteric LN; PBL, peripheral blood lymphocytes; SPL, spleen.

immunoglobulin mucin (Tim-3); BioLegend, San Diego, CA], and allophycocyanin-H7 anti-CD4 (BD Bioscience, Becton Dickinson GmbH, Heidelberg, Germany). Cells were stained for 30 minutes on ice, washed, and fixed with CellFIX (BD Bioscience, Becton Dickinson GmbH). Flow cytometric data were acquired using an LSR II flow cytometer (BD Bioscience, Becton Dickinson GmbH) or CytoFLEX S (Beckman Coulter, Brea, CA) and analyzed using FlowJo version 10 (Tree Star, Ashland, OR). To obtain the absolute cell counts, the total number of viable cells counted after homogenization of the tissues was divided by the percentage of the specific cell population after flow cytometry analyses.

Infection of Humanized Mice with EBV

After confirmed human hematopoietic engraftment in peripheral blood 15 to 17 weeks after HSCT, mice were randomized on the basis of the levels of T-cell reconstitutions between control and EBV-infected groups. For EBV infections, mice were injected via the tail vein with 10^5 GFP Raji infectious units of EBV-B95.8/fLuc2 or EBV-B95.8/GFP diluted in 100 μL phosphate-buffered saline. Weight monitoring after infections was performed weekly. Euthanasia was performed if symptoms of distress due to tumor development were detected or 10 weeks after EBV infections.

Optical and Computed Tomographic Imaging Analysis of EBV-Infected Mice

Mice infected with EBV-B95.8/fLuc2 were analyzed for luciferase expression using an IVIS SpectrumCT apparatus (PerkinElmer, Waltham, MA). In brief, mice were anesthetized using isoflurane. Five minutes before imaging, 2.5 mg D-luciferin potassium salt (SYNCHEM, Elk Grove Village, IL) dissolved in 100 μL phosphate-buffered saline was administered intraperitoneally. For three-dimensional reconstruction of the bioluminescent signal, micro—computed tomographic data were acquired at the same time as acquisition of the optical data. Data were analyzed using the LivingImage Software version 4.5 (PerkinElmer).

Quantification of EBV by Real-Time Quantitative PCR

DNA was extracted from whole spleen specimens using the DNeasy Blood & Tissue Kit (Qiagen, Venlo, the Netherlands), according to the manufacturer's protocol. Quantification of EBV DNA was performed by amplifying a fragment

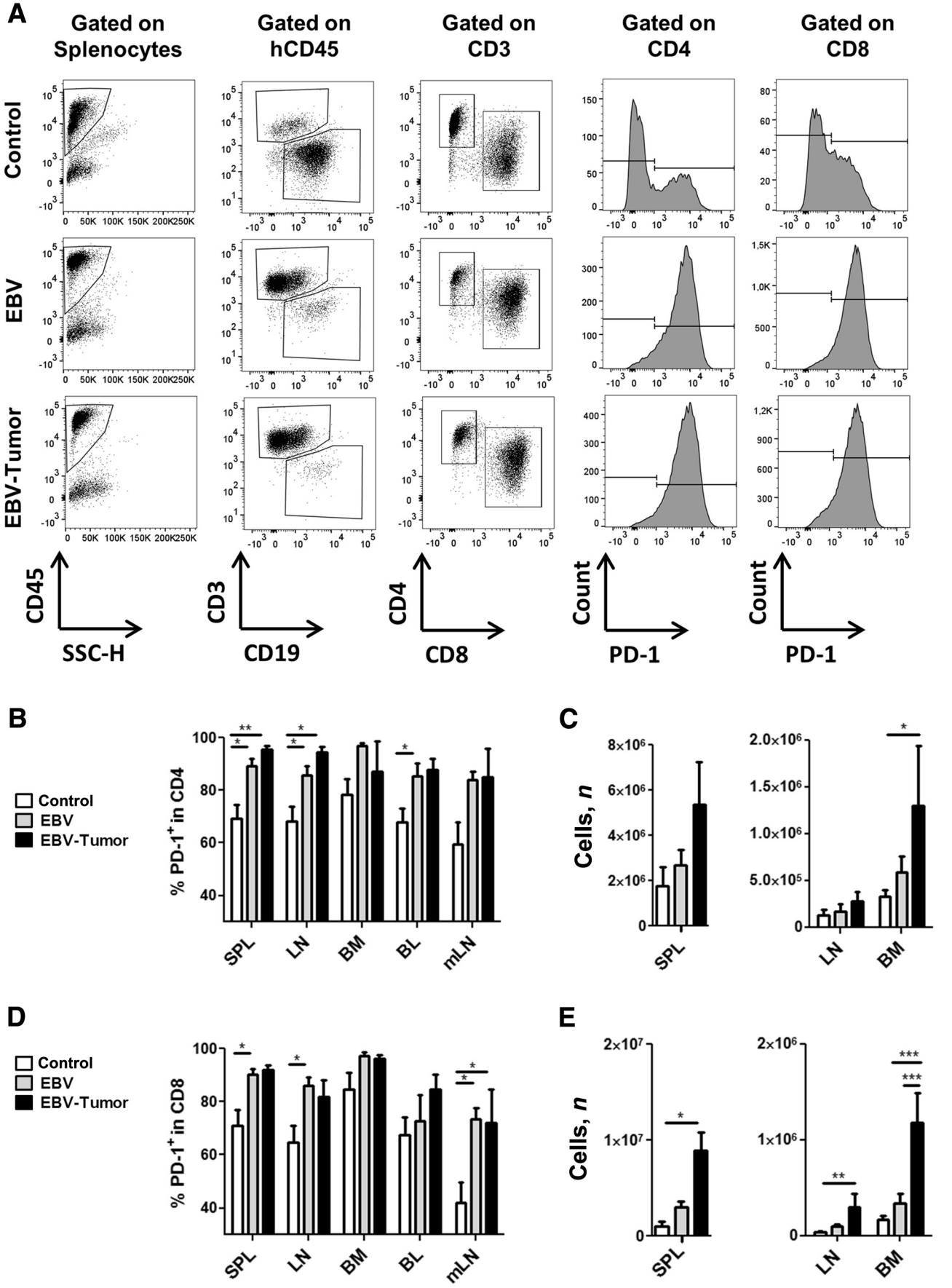
A
Gated on Splenocytes
Gated on hCD45
Gated on CD3
Gated on CD4
Gated on CD8
Control
EBV
EBV-Tumor
CD45
SSC-H
CD3
CD19
CD4
CD8
Count
PD-1
Count
PD-1
B
Control
EBV
EBV-Tumor
% PD-1+ in CD4
SPL
LN
BM
BL
mLN
C
Cells, n
SPL
LN
BM
D
Control
EBV
EBV-Tumor
% PD-1+ in CD8
SPL
LN
BM
BL
mLN
E
Cells, n
SPL
LN
BM

of the *BALF4* gene using the following primers: forward, 5′-CTTTGGCGCGGATCCTC-3′; and reverse, 5′-AGTCCTTCTTGGCTAGTCTGTTGAC-3′. Amplification was detected by using the following TaqMan probe: 5′-Fam-CATCAAGAAGCTGCTGGCGGCC-Tamra-3′. For reaction, 5 μL of DNA was added to 20 μL of TaqMan 2× Universal Mastermix (Thermo Fisher Scientific) containing 2.5 μL of each primer (2 μmol/L), 1 μL of TaqMan probe (5 μmol/L), and 1.5 μL of PCR-grade nuclease-free water. PCRs were run with the StepOnePlus Real-Time System (Applied Biosystems, Life Technologies, Darmstadt, Germany) using the following cycling conditions: 2 minutes at 50°C, 10 minutes at 95°C, 40 cycles of 15 seconds at 95°C, and 1 minute at 56°C. Data were analyzed using the StepOnePlus software version 2.3 (Applied Biosystems, Life Technologies).

Detection of IFN-γ–Secreting T Cells by ELISpot

EBV-specific interferon (IFN)-γ–producing T lymphocytes were enumerated by IFN-γ ELISpot using T-track human Kit according to the vendor's recommendations (Lophius Biosciences, Regensburg, Germany), as described previously.[29] Briefly, viable mononuclear cells obtained from tissues of humanized mice ($n = 3$ for each cohort), peripheral blood from EBV-seropositive donors ($n = 3$), or cord blood ($n = 3$) were plated at a density of 2.5×10^5 cells per well and incubated overnight with 2.5 μg/mL CEF peptide pool as a positive control, ppBZLF1 peptide pool (1 μg/mL propeptide), and T-activated EBNA3A and BZLF1-protein, respectively (2 μL each; both from Lophius Biosciences). Untreated cells served as negative control spot-forming units and were counted and analyzed using the AID iSpot Spectrum Reader (AID, Straßberg, Germany). A spot count at least two times higher than the spot count of the negative control was regarded positive.

Histopathology, Immunohistochemistry, and Image Analysis

Formalin-fixed, paraffin-embedded tissues were divided into sections (3 μm thick) and stained according to standard protocols for hematoxylin-eosin and Giemsa. Immunohistochemistry using the Benchmark Ultra automated instrument (Ventana/Roche Tissue Diagnostics, Mannheim, Germany) was performed for staining: CD8 (clone C8/144B; Dako, Copenhagen, Denmark), CD4 (clone SP35; Zytomed Systems, Berlin, Germany), PD-1 (MRQ-22; Medac Diagnostika, Wedel, Germany), CD30 (Ber-H2; Dako), and programmed cell death ligand 1 (PDL-1; clone 22C3; Dako). The 3,3′-diaminobenzidine–based UltraView detection reagent was used following the manufacturer's recommendations. EBV-infected cells were detected by *in situ* hybridization using the EBER 1 DNP Probe (Ventana/Roche Tissue Diagnostics; designed to bind to EBV-encoded *RNA 1*, EBER 1) and the automated Benchmark Ultra instrument. Staining results were evaluated visually, and images were taken on the Olympus BX46 microscope (Olympus Europe, Hamburg, Germany). In addition, CD4, CD8, PD-1, and EBER staining was evaluated using Mantra Quantitative Pathology Workstation, including the inForm software version 2.4.1 (Perkin Elmer, Rodgau, Germany). Three to five visually selected fields of view acquired with the 20× objective were subjected to color deconvolution by multispectral imaging. The perivascular lymphocytic infiltrate was manually annotated. Computational color deconvolution was used to separate color channels (black/dark blue for *in situ* hybridization, blue for hematoxylin, and 3,3′-diaminobenzidine/brown for CD4, CD8, and PD-1). Segmentation and classification of image objects using the inForm cell phenotyping tool resulted in accurate detection of EBER-positive nuclei (*in situ* hybridization), which were recorded as number of stained nuclei per area (in pixels). The density of immune cells (corresponding to the relative number of CD4-, CD8-, and PD-1–positive cells by immunohistochemistry) was estimated regarding positively stained image objects per area (in pixels).

Statistical Analysis

For these proof-of-concept experiments, data acquisition was not blinded and sample sizes were not statistically determined before experiments. Statistical analysis was performed using the GraphPad Prism software versions 6 and 7 (GraphPad Software Inc., La Jolla, CA). One-way analysis of variance with Tukey post-test for multiple comparisons was used to calculate statistical significance. $P < 0.05$ was considered statistically significant.

Results

Infection of Humanized Mice with EBV-B95.8/fLuc2, Monitored by Noninvasive Optical Imaging Analysis and Computed Tomography, Shows Exponential and Systemic EBV Burst

Before *in vivo* use, the titers of EBV viral batches were tested by *in vitro* infection and immortalization of primary B

Figure 5 End point analyses of frequencies and absolute counts of the PD-1$^+$ human T cells in different tissues. Bars filled with white, gray, and black represent control, Epstein-Barr virus (EBV), and EBV-Tumor cohorts, respectively. **A:** Gating strategy for analyses of PD-1 expression on CD4$^+$ and for CD8$^+$ cells. **B:** Frequencies of PD-1$^+$/CD4$^+$ for spleen (SPL), lymph nodes (LNs), mesenteric lymph nodes (mLNs), bone marrow (BM), and blood (BL). **C:** Absolute cell numbers of PD-1$^+$/CD4$^+$ for spleen, lymph nodes, and bone marrow. **D:** Frequencies of PD-1$^+$/CD8$^+$ for SPL, LNs, mLNs, BM, and BL. **E:** Absolute cell numbers of PD-1$^+$/CD4$^+$ for spleen, lymph nodes, and bone marrow. The sample sizes per tissues are shown in Supplemental Table S1. $^*P < 0.05$, $^{**}P < 0.01$, and $^{***}P < 0.001$. hCD45, human CD45; K, 1000; SSC, side scatter.

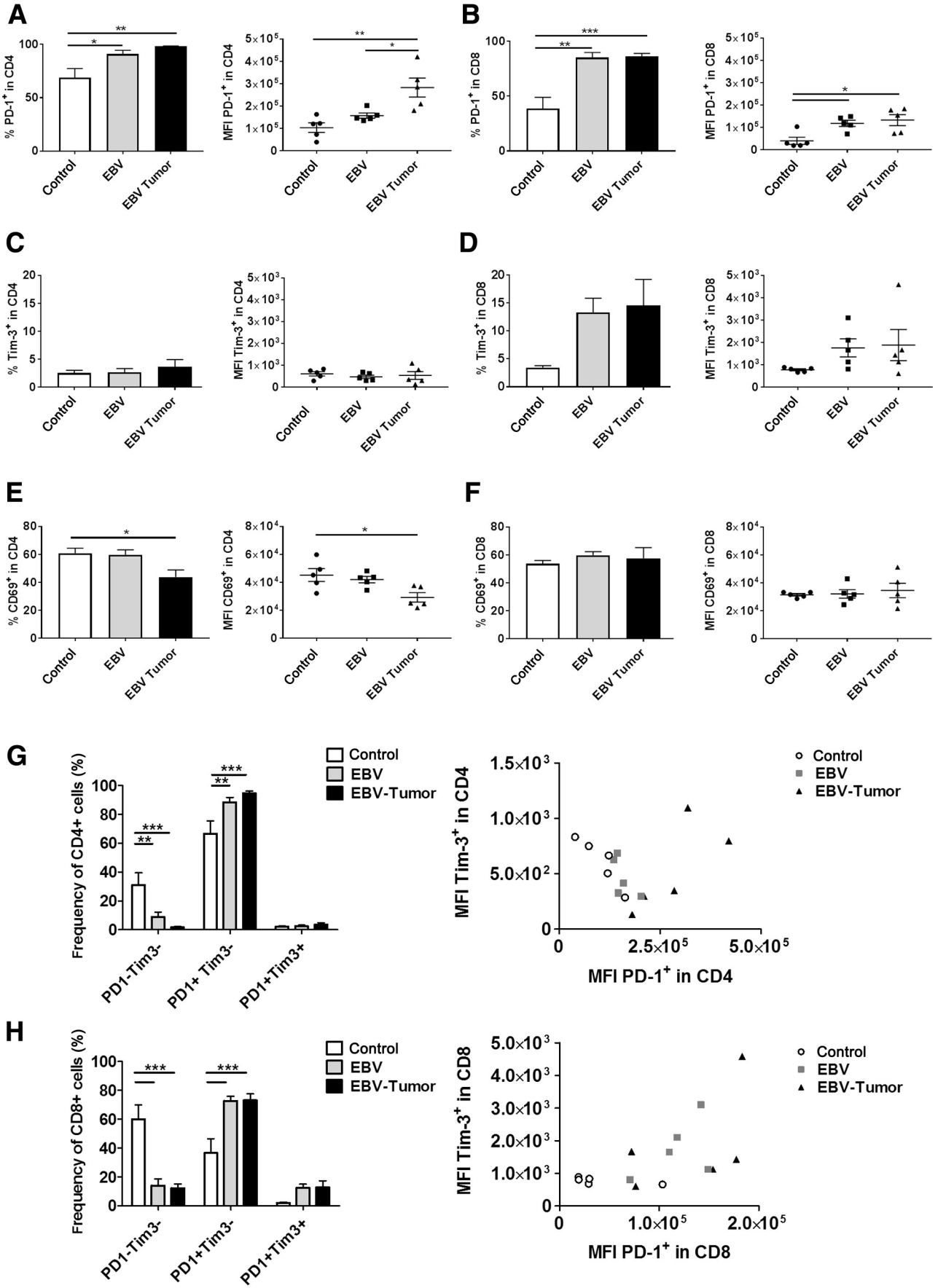
A
% PD-1+ in CD4
MFI PD-1+ in CD4
B
% PD-1+ in CD8
MFI PD-1+ in CD8
C
% Tim-3+ in CD4
MFI Tim-3+ in CD4
D
% Tim-3+ in CD8
MFI Tim-3+ in CD8
E
% CD69+ in CD4
MFI CD69+ in CD4
F
% CD69+ in CD8
MFI CD69+ in CD8
Control
EBV
EBV Tumor
G
Frequency of CD4+ cells (%)
PD1-Tim3-
PD1+ Tim3-
PD1+Tim3+
Control
EBV
EBV-Tumor
MFI Tim-3+ in CD4
MFI PD-1+ in CD4
H
Frequency of CD8+ cells (%)
PD1-Tim3-
PD1+Tim3-
PD1+Tim3+
MFI Tim-3+ in CD8
MFI PD-1+ in CD8

cells. EBV-transformed lymphoblastoid cell lines showed detectable expression of PD-L1 and PD-1 on the cell surface (Figure 1A). Fifteen weeks after huHSCT using CD34$^+$ cells from three individual CB donors, mice were infected via tail vein injection with EBV-B95.8/fLuc2 or EBV/GFP (10^5 GFP Raji infectious units). Mice were sacrificed 10 weeks later or earlier if signs of disease became evident (Figure 1B). Optical imaging for tracking the biodistribution of the EBV-B95.8/fLuc2 infections showed a faint bioluminescence signal restricted to the anatomic region of spleen 1 week after infection, which then increased exponentially until 5 weeks after infection (Figure 1, C and D). At this point, when the bioluminescence signals were conspicuous, three-dimensional high-resolution optical imaging combined with computed tomography showed hotspots of EBV-infected cells dispersed in regions of the spleen and adjacent lymph nodes (Figure 1E and Supplemental Video S1). Optical imaging analyses performed after euthanasia and inspection of the organs by optical imaging analyses showed pronounced bioluminescent signals in spleen, lymph nodes, lungs, liver, and salivary glands (Figure 1F).

EBV-B95.8/GFP Infection and Tumor Development Changes the Kinetics of Human Immune Cell Reconstitution in Blood, Skewing toward Significantly Higher Frequencies of CD8$^+$ T Cells

Mice transplanted with CD34$^+$ cells obtained from several CB donors were used to replicate independent experiments for comparisons between noninfected controls ($n = 19$) and EBV-B95.8/GFP infected ($n = 18$) (Table 1). Among EBV-infected mice, 8 of 18 (44%) developed macroscopically visible tumors in the spleen. For further analyses of the data, EBV-infected mice were then compared with (EBV-Tumor) or without (EBV) macroscopic tumors (Table 1). All mice showed detectable human CD45$^+$ cells in the peripheral blood until euthanasia (ie, 25 to 27 weeks after huHSCT), but although control mice consistently showed a gradual reduction in the frequencies of human CD45$^+$ cells over time, EBV-infected mice showed more variable patterns (Figure 2, A and B). Regarding the kinetics of B and T lymphocytes, CD19$^+$ B cells predominated at the time of infection, but their frequencies gradually decreased over time for all groups (Figure 2, C and D). Remarkably, this decrease was significantly more pronounced at 6 weeks after infection for EBV-infected mice compared with controls (control versus EBV: $P = 0.0102$; control versus EBV-Tumor: $P = 0.0007$) (Figure 2D). Concurrently, EBV-infected mice showed a significantly faster expansion of CD3$^+$ T cells compared with noninfected mice (control versus EBV: $P = 0.0165$; control versus EBV-Tumor: $P = 0.0056$) (Figure 2E). Although the frequency of CD4$^+$ T cells within human CD45$^+$ cells in blood slightly decreased after EBV infection relative to controls (control versus EBV: $P = 0.77$; control versus EBV-Tumor: $P = 0.38$) (Figure 3, A and B), the relative CD8$^+$ T-cell frequencies increased significantly and constantly (control versus EBV: $P = 0.0021$; control versus EBV-Tumor: $P \leq 0.0001$; EBV versus EBV-Tumor: $P = 0.0072$) (Figure 3, A and C).

EBV-B95.8/GFP Infection Followed by Tumor Development Significantly Stimulates the Expansion of CD8$^+$ T Cells in Lymphatic Tissues

Tumor development was associated with higher frequencies of CD8$^+$ T cells within human CD45$^+$ cells in blood and lymphatic tissues (mLN, spleen, and BM) (Table 2 and Figure 4, A–C, E, and G). Nonetheless, in terms of absolute cell counts, the increases were more dramatic in EBV-Tumor mice. These differences amounted to approximately 10-fold relative to controls and threefold relative to mice not developing tumors for spleen (control versus EBV: $P = 0.45$; control versus EBV-Tumor: $P \leq 0.0001$; EBV versus EBV-Tumor: $P = 0.0023$) (Figure 4D), LN (control versus EBV: $P = 0.67$; control versus EBV-Tumor: $P = 0.003$; EBV versus EBV-Tumor: $P = 0.04$) (Figure 4F), and BM (control versus EBV: $P = 0.45$; control versus EBV-Tumor: $P \leq 0.0001$; EBV versus EBV-Tumor: $P = 0.0007$) (Figure 4H). Compared with CD8$^+$ T cells, the increase in the absolute CD4$^+$ T-cell counts in EBV-Tumor mice relative to controls or EBV mice without tumors was not so pronounced (Table 2 and Figure 4, D, F, and H).

Analysis of PD-1 Expression on T Cells Obtained from Different Lymphatic Tissues

The frequencies of PD-1–expressing CD4$^+$ and CD8$^+$ T cells were analyzed by quantitative flow cytometry (Figure 5A). For control mice, the frequencies of PD-1$^+$ CD4$^+$ and PD-1$^+$ CD8$^+$ T cells were 20% to 40% in mLNs and 85% to 90% in BM (Figure 5, B and D, and Supplemental Table S1). In contrast, mice infected with EBV showed 90% to 100% of the CD4$^+$ and CD8$^+$ T cells in

Figure 6 Single and combined analyses of frequencies of CD4$^+$ and CD8$^+$ and respective mean fluorescence intensities (MFIs) of PD-1, Tim-3, and CD69 on T cells obtained from lymph nodes. **A** and **B:** Analyses of PD-1 on CD4$^+$ (**A**) and CD8$^+$ (**B**) T cells. **C** and **D:** Analyses of Tim-3 on CD4$^+$ (**C**) and CD8$^+$ (**D**) T cells. **E** and **F:** Analyses of CD69 on CD4$^+$ (**E**) and CD8$^+$ (**F**) T cells. **G:** Combined analysis of CD4$^+$ T cells. Panel with bar graphs on the left depicts combined analyses of PD-1 and Tim-3 (Tim-3$^-$PD-1$^-$ defined phenotypically as functional, Tim-3$^-$PD-1$^+$ defined as partially dysfunctional, Tim-3$^+$PD-1$^+$ defined as severely dysfunctional). Panels with MFI for PD-1 (*x* axis) and MFI for Tim-3 (*y* axis) showing relationship between expression levels of both markers for each cohort. **H:** Similar combined analysis for CD8$^+$ T cells. $n = 5$ mice per cohort [control, Epstein-Barr virus (EBV)–infected mice, and EBV-infected mice developing tumors]. $^*P < 0.05$, $^{**}P < 0.01$, and $^{***}P < 0.001$.

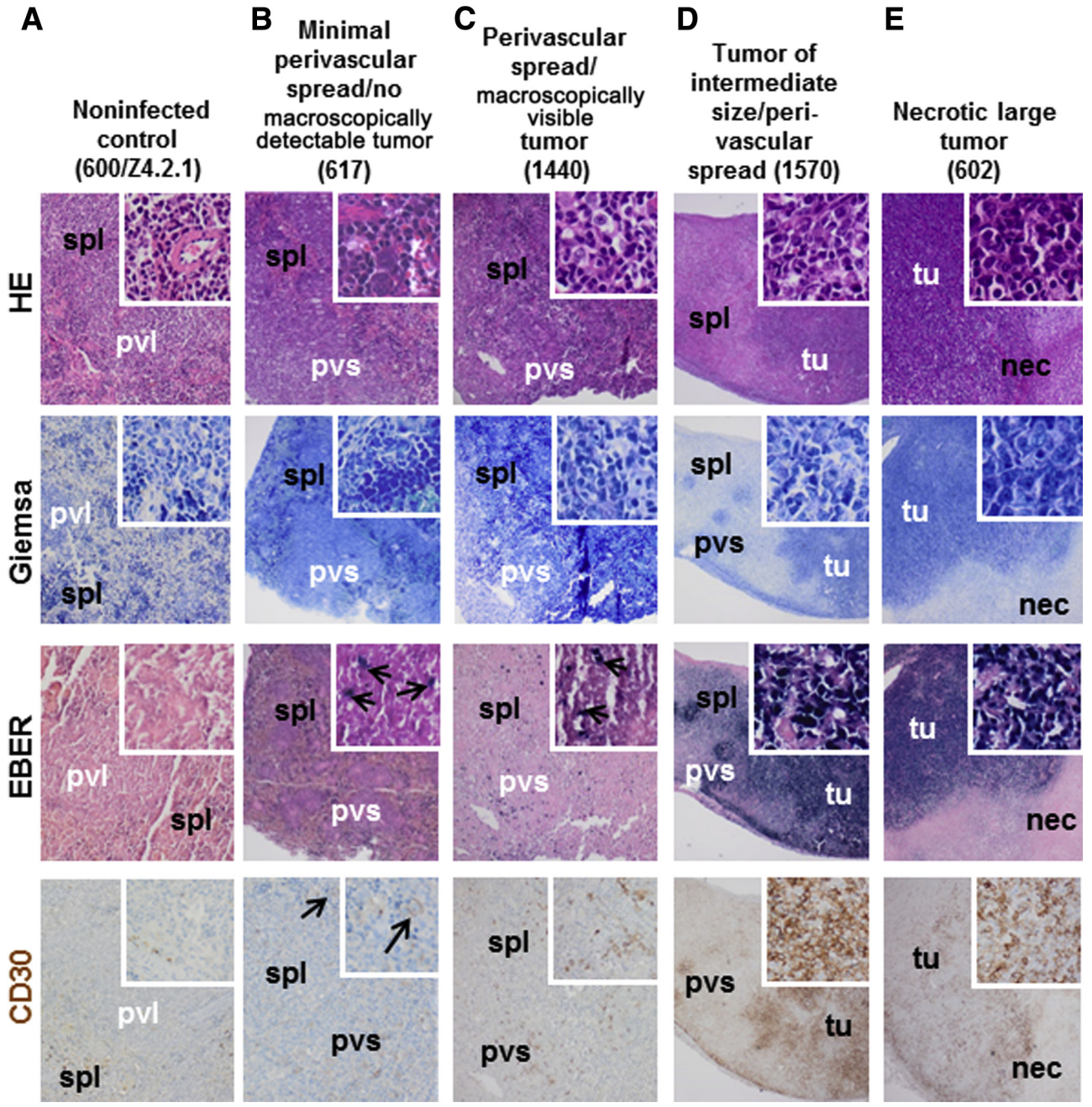

Figure 7 Histopathological analysis of four exemplary samples of splenic tissue analyzing spread of Epstein-Barr virus (EBV)—positive cells and formation of tumor. Hematoxylin-eosin (HE), Giemsa, EBER, and CD30 are shown. **Arrows** indicate positive staining signals. **A:** Representative example for staining of spleen of an uninfected control humanized mouse. **B:** Detection of few EBV-positive cells in minimal perivascular spread (pvs) in the spleen (spl) in a representative example for the EBV-infected group without macroscopically detectable tumors. **C:** Representative example of splenic perivascular spread of EBV-positive and CD30-expressing cells in an animal that developed a macroscopically visible tumor elsewhere. **D:** Tumor (tu) formation of intermediate size in the spleen. Note the densely packed EBV-positive cells (as detected by EBER *in situ* hybridization) in the tu area, whereas the adjacent spl tissue shows the pvs. **E:** Example of a large partially necrotic (nec) tumor. Preexisting spl, pvs, tu, and nec regions are shown. **A**—**C**, 10× objective; **D** and **E**, 4× objective; **insets**, 40× objective. pvl, perivascular lymphocytes.

lymphatic tissues expressing PD-1 (Figure 5, B and D, and Supplemental Table S1). Regarding absolute T-cell numbers, mice with EBV tumors showed twice as many PD-1^+ $CD4^+$ and three times as many $CD8^+$ T cells as infected mice without tumors (Table 2, Figure 5, C and E, and Supplemental Table S1). Data were found in spleen (control versus EBV: $P = 0.91$; control versus EBV-Tumor: $P = 0.02$; EBV versus EBV-Tumor: $P = 0.06$), LN (control versus EBV: $P = 0.45$; control versus EBV-Tumor: $P = 0.0043$; EBV versus EBV-Tumor: $P = 0.07$), and

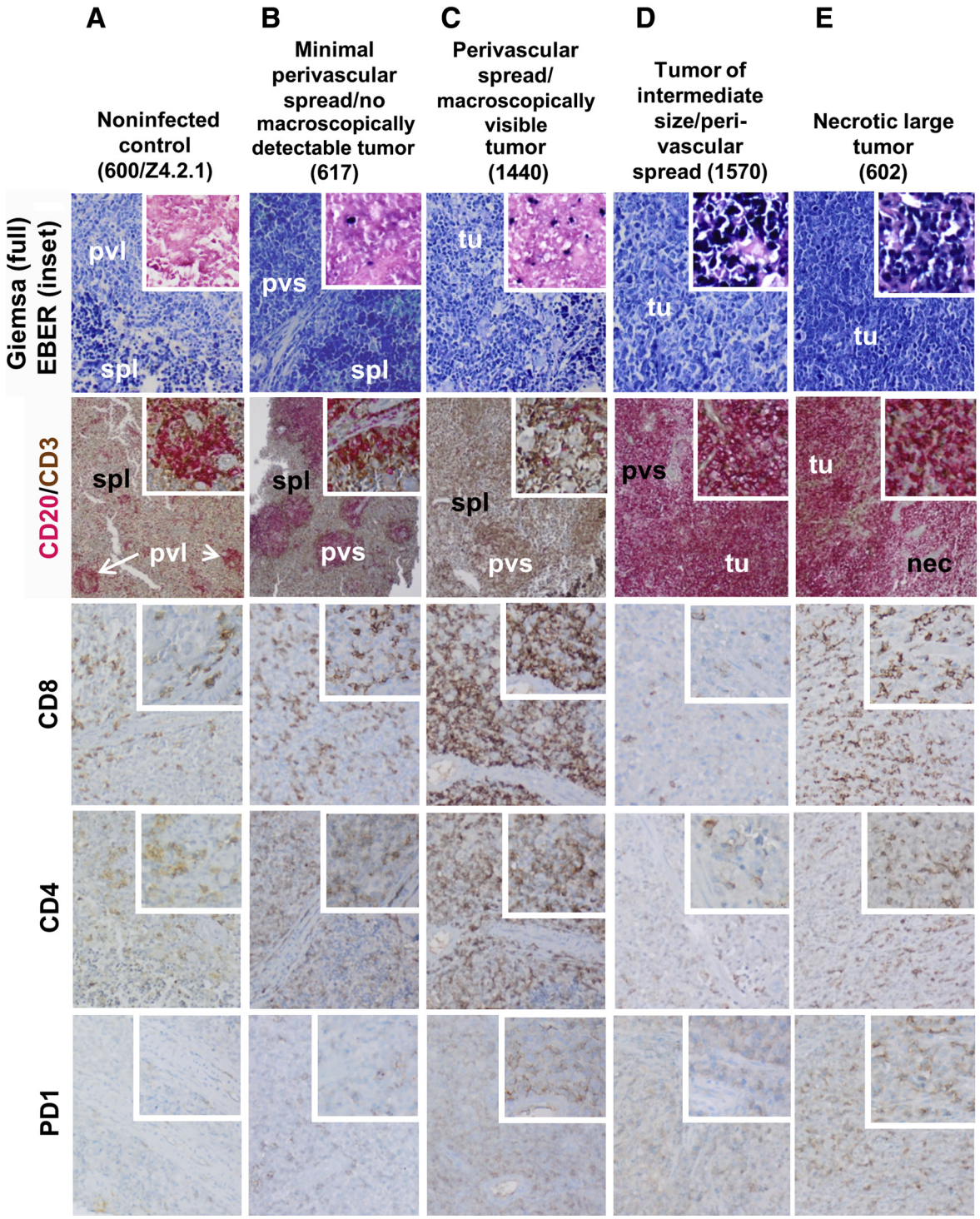

Figure 8 Histopathological analysis of representative samples of splenic tissue characterizing immune cell infiltration in context of Epstein-Barr virus (EBV)—positive cell spread and tumor formation (Giemsa, EBER, CD20/CD3 duplex staining, CD8, CD4, and PD-1). **A:** Representative staining of a spleen of an uninfected control humanized mouse. **B**—**D:** EBV-infected humanized mice. **B**—**E:** Perivascular spread and tumor formation of EBV-infected cells was associated with a T-cell—rich infiltrate. **B:** In cases with minimal perivascular spread, a few EBV-positive cells are mixed with presumably preexisting B cells in the humanized splenic microenvironment and are surrounded by a moderate mixed T-cell infiltrate with low fractions of PD-1 positivity. **C:** In cases with more advanced perivascular spread, the infiltrates associated with the EBV-infected cells consist predominantly of T cells, of both CD4$^+$ and CD8$^+$ phenotype, with increasing fractions of PD-1—expressing cells. CD20$^+$ cells in this microenvironment could be remnants of preexisting splenic tissue or invading CD20-expressing EBV-infected cells. **D:** The case with an intermediate-sized splenic tumor shows massive perivascular spread of CD20$^+$ blasts, colocalizing with the EBV-positive cell population and surrounded by PD-1$^+$ T cells. The images show an area within the tumor formation, with strikingly low numbers of T cells. **E:** The case with a large necrotic tumor shows a more prominent T-cell infiltrate with substantial PD-1 expression. Preexisting splenic (spl) tissue, perivascular spread (pvs), tumor (tu), and necrotic (nec) regions are shown. **Top two rows**, 10× objective; **bottom three rows**, 20× objective; **insets**, 40× objective. pvl, perivascular lymphocytes.

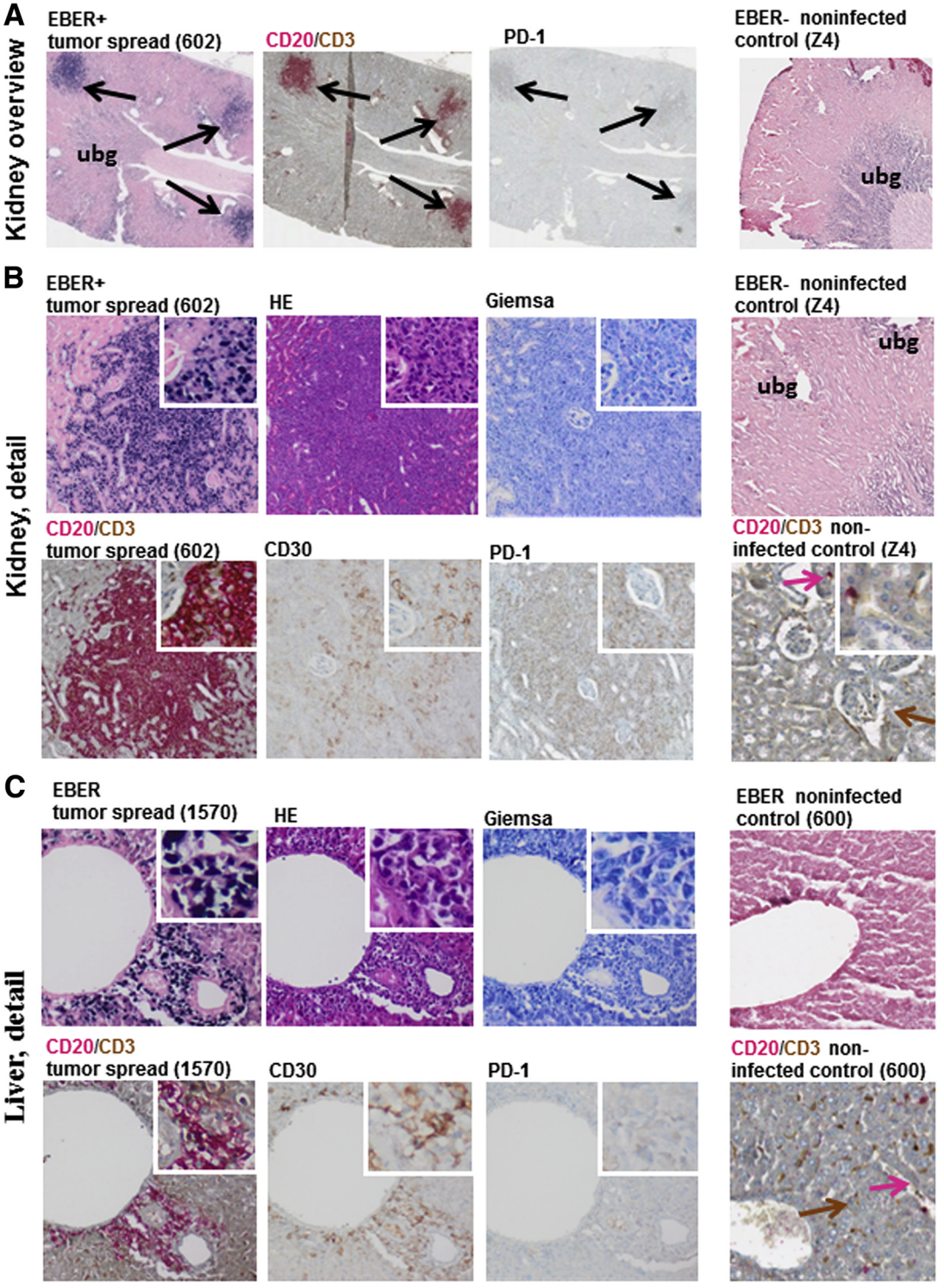

Figure 9 Histopathological analysis of extrasplenic spread in kidney and liver in the Epstein-Barr virus (EBV)—infected tumor-bearing group. Hematoxylin-eosin (HE), Giemsa, CD30, EBER, CD20, CD3, and PD-1 are shown. **A**—**C:** Histopathological investigation reveals subtle tumor-like spread of EBV-positive blasts into several organs, of which staining of kidney tissue (**A** and **B**) and liver tissue (**C**) is shown as an example. **Right column:** Examples of staining of the corresponding tissue of a noninfected control. The automated EBER *in situ* hybridization produced some diffuse unspecific background staining (ubg) that was not nuclear and clearly distinguishable from specific nuclear staining by coloring and density. **A:** Multiple spread of tumors in the kidney is associated with blood vessels and shows colocalization between EBER hybridization signal, $CD20^{+}$ cells with blast morphology, and PD-1—expressing T-cell infiltrates (**arrows**). **B:** Higher magnification reveals the morphology of an EBV-positive neoplasia of B-cell origin with CD30 expression in most blast-like cells. It is accompanied by a dense infiltrate of PD-1—expressing cells. **C:** A similar pattern can be observed in a different case, with mostly perivascular spread of a blast-like hematological neoplasia with CD20 and CD30 coexpression and an accompanying infiltrate containing PD-1—positive T cells. The **pink arrows** indicate a positive CD20 staining signal; **brown arrow**, a positive CD3 staining signal. **A**, 10× objective; **B** and **C**, 20× objective; **insets**, 40× objective.

BM (control versus EBV: $P = 0.38$; control versus EBV-Tumor: $P \leq 0.0001$; EBV versus EBV-Tumor: $P = 0.0002$).

Combined Analysis of PD-1/Tim-3 and PD-1/CD69 Expression by T Cells from LNs

To further characterize the activation and potential dysfunctional status of the T cells on chronic EBV infection, the expression of PD-1 was examined in combination with Tim-3 or CD69 by multicolor flow cytometry analyses. Previously, double-negative Tim-3$^-$PD-1$^-$CD8$^+$ cytotoxic T lymphocytes (CTLs) were classified as functional CTLs, whereas single-negative Tim-3$^-$PD-1$^+$ and double-positive Tim-3$^+$PD-1$^+$ were previously defined to be partially dysfunctional and severely dysfunctional, respectively.[30] Mononuclear cells obtained from lymph nodes of noninfected control mice ($n = 5$), EBV-infected mice ($n = 5$), and EBV-infected mice with tumor development ($n = 5$) were analyzed in parallel. Similar to previous observations (Figure 5, B–E), compared with controls, all mice infected with EBV showed significantly higher frequencies of PD-1$^+$ CD4$^+$ and CD8$^+$ T cells (Figure 6, A and B). A significant up-regulation of PD-1 expression was observed for EBV-infected mice developing tumors (CD4$^+$ T cells: control versus EBV-Tumor: $P = 0.002$; EBV versus EBV-Tumor: $P = 0.026$; CD8$^+$ T cells: control versus EBV: $P = 0.036$; control versus EBV-Tumor: $P = 0.013$) (Figure 6, A and B). Unlike PD-1, expression of the inhibitory receptor Tim-3 on CD4$^+$ T cells was comparable among all cohorts, both for cell frequencies and levels of expression (Figure 6C). In contrast, the frequency of Tim-3$^+$ CD8$^+$ T cells was three times higher for mice infected with EBV (without or with tumors) compared with controls, and this was also associated with up-regulation of Tim-3 expression (Figure 6D). As a reference marker to assess T-cell activation solely, CD69, a classic early marker of lymphocyte activation, was explored.[31] The frequency of CD69$^+$CD4$^+$ T cells was significantly lower for the cohort of mice developing tumors (40%) compared with controls (approximately 60%), and this was also associated with lower expression levels (control versus EBV-tumor: $P = 0.024$) (Figure 6E). On the other hand, CD69 expression on CD8$^+$ T cells was similar for all of the cohorts (Figure 6F). These findings indicated that expression of the activation marker CD69 was uncoupled with the transcriptional program, resulting in PD-1 up-regulation and symptomatic dysfunction. The analyses of the two coinhibitory receptors Tim-3 and PD-1 were subsequently linked to define the functional status of T cells subjected to chronic stimulation with EBV antigens. A significant decrease was found in frequencies of the double-negative CD4$^+$ and CD8$^+$ Tim-3$^-$PD-1$^-$ functional T-cell subpopulation on EBV infection (CD4$^+$: control versus EBV: $P = 0.004$; control versus EBV-Tumor: $P = 0.000$; CD8$^+$: PD-1$^-$Tim-3$^-$: control versus EBV: $P \leq 0.0001$; control versus EBV-Tumor: $P < 0.0001$), and a significant increase was found in the single-negative Tim-3$^-$PD-1$^+$ partially dysfunctional subpopulation for CD4$^+$ cells (control versus EBV: $P = 0.004$; control versus EBV-Tumor: $P = 0.0002$) (Figure 6G). Even more pronounced effects were observed for CD8$^+$ cells (control versus EBV: $P = 0.0002$; control versus EBV-Tumor: $P = 0.0002$) (Figure 6H). Severely dysfunctional double-positive Tim-3$^+$ PD-1$^+$ CD4$^+$ cells were rare, and comparable among all groups (Figure 6G). However, the frequencies of double-positive cells were substantially elevated for CD8$^+$ cells when mice were infected with EBV (greater than fivefold; frequency mean: control = 2.068%; EBV = 12.42%; EBV-Tumor = 12.87%; although not statistically significant differences) (Figure 6H). For CD4$^+$ cells, Tim-3 expression level (y axis) plotted relative to the PD-1 expression level (x axis) showed clustering of the mice developing tumors farther away from the other two cohorts (Figure 6G). When this analysis was applied to CD8$^+$ T cells, the noninfected cohort clustered clearly separately from the EBV-infected and EBV with tumor cohorts (Figure 6H). In sum, on the basis of these combined immune phenotypic analyses of Tim-3 and PD-1 expression, EBV infection conclusively affected the functionality of T cells, and this was more pronounced for CD8$^+$ T cells. Furthermore, to examine whether functional responses against EBV-specific antigens were detectable, IFN-γ ELISpot analysis was performed. Mononuclear cells were obtained from three EBV-seropositive healthy human donors (peripheral blood mononuclear cells), three EBV-seronegative CB units, and three mice per cohort (using cryopreserved/thawed bone marrow samples). T-cell responses against the Epstein-Barr virus nuclear antigen 3 (EBNA3, recombinant protein) and BZLF1 (recombinant protein and peptide pool) were not detectable for the CB negative control and validated for all positive control healthy human donor subjects (Supplemental Figure S1). In contrast, only T cells from one EBV-infected mouse developing tumor showed a trustworthy T-cell response (Supplemental Figure S1). Despite the limitations of IFN-γ ELISpot assays applied to humanized mice, these results further ratified that although human T cells expanded dramatically after EBV infection and development of tumors in humanized mice, they seemed to be dysfunctional.

In Situ Analysis of EBV Infection and Extent of Tumor Spread in Spleen

Histopathological analyses of tissues and tumors were performed in 14 cases, arbitrarily selected to cover the full range of changes observed in the experimental setting. These cases represented four noninfected controls (188, 600, Z4, and Z10), four EBV-infected humanized mice without visible tumors on macroscopic inspection (referred to as EBV 604, 615, 617, and 1014), and six EBV-infected humanized mice with macroscopically visible locoregional tumors in different organs (referred to as EBV-Tumor 187, 602, 1015, 1440, 1510, and

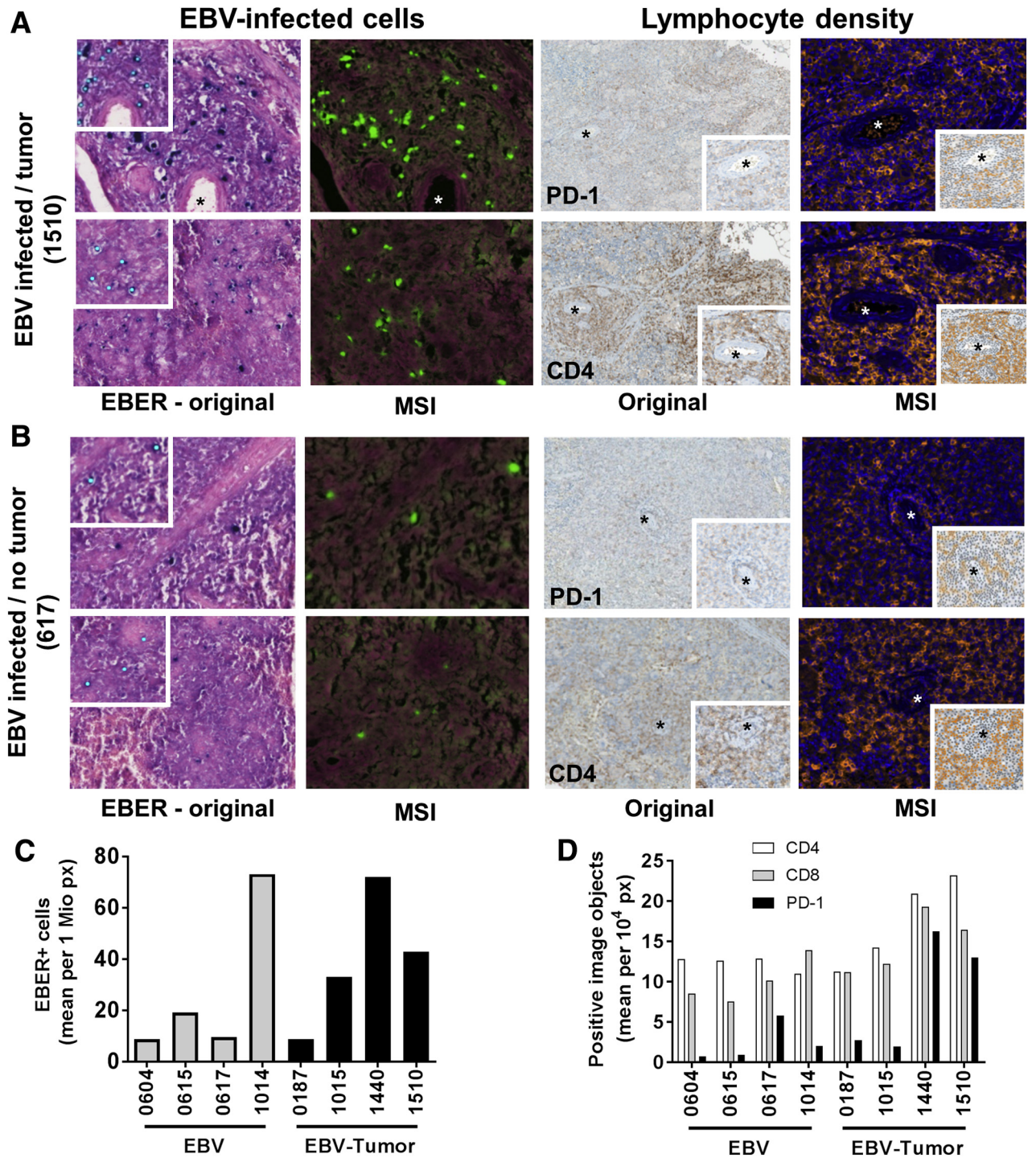

Figure 10 Automated quantification of Epstein-Barr virus (EBV)—infected cells and evaluation of stained image objects representing CD4-, CD8-, and PD-1—positive immune cells. The quantitative assessment of EBV-positive cells in zones of perivascular spread (EBV-infected cells) and the estimation of immune cell infiltration (lymphocyte density) revealed strikingly variable infiltrates with a trend toward increased density of PD-1^+ T cells particularly in two cases (1440 and 1510) with a high perivascular load of EBV-infected cells. **A:** Representative example for perivascular spread of EBER-positive cells in an animal that developed macroscopically visible tumors elsewhere (1510). EBV-infected cells: In the brightfield (original) images, the EBER—*in situ* hybridization positive cells are stained in dark blue. The false color images generated after deconvolution by multispectral imaging (MSI) highlight the detected positive nuclei in green. The result of the automated EBV cell detection (positive nuclei marked by blue dots) is shown in the **insets** of the original image. Lymphocyte density: PD-1 and CD4 immunohistochemistry showing perivascular accumulation of positive cells in the original image and after deconvolution by MSI. The result of automated quantification of image objects that correspond to PD-1— and CD4-positive immune cells is shown in the **insets** of the MSI image. **B:** Corresponding image analysis in an EBV-infected case without macroscopically visible tumor burden shows few EBER-positive cells (617), showing a moderate perivascular PD-1^+ infiltrate higher than in other cases without visible tumor load, but clearly lower than in the tumor-bearing cases 1510 and 1440. **Asterisks** indicate center of a blood vessel. **C** and **D**: The comparison between quantity of EBER positive cells (**C**) and immune cell infiltrates (**D**), confirming variability across different animals in both the tumor-free and the tumor-bearing population. EBV-infected cells, 40x objective; lymphocyte density original, 10x objective; lymphocyte density MSI, 20x objective. px, pixel.

1570). Microscopic evaluation showed different stages of predominantly perivascular spread of EBV-infected cells. Noninfected control mice were used as reference (Figure 7A). For display, four representative examples of EBV-infected mice, illustrating different grades of severity, were chosen. The grades of severity included: minimal presence of EBV-infected cell infiltrates and no visible macroscopic tumor (Figure 7B); increased splenic perivascular spread of EBER-positive cells in cases with macroscopically visible tumors in a different location (Figure 7C); splenic tumors that appeared to be progressive stages of increased perivascular spread of EBV-positive lymphoproliferative neoplasia (Figure 7D); and a necrotic large tumor in spleen, where the preexisting murine splenic tissue and the spatially organized inflammatory reaction of human normally sized immune cells of T- and B-cell origin were almost completely replaced by the lymphoproliferative lesion (Figure 7E).

In Situ Analysis of the Inflammatory Microenvironment in Context of EBV Infection

In the representative cases corresponding to different grades of disease spread, the lymphoproliferative lesion was characterized by a consistent lymphoid blast–like morphology and frequent CD20/CD30 coexpression (Figures 7 and 8), and it was associated with different densities of infiltrating CD3$^+$ T cells (Figure 8). Further immunophenotyping of these T-cell infiltrates in close proximity to EBV-positive cells revealed variable numbers of CD8$^+$ and CD4$^+$ T cells, with a peak of CD8$^+$ cells in areas of high EBV density, and a striking colocalization of EBV-positive cells and the abundance of PD-1$^+$ cells (Figure 8). This pattern was most obvious in splenic tissue. Nevertheless, human T-cell infiltrations into kidney and liver showed similar trends. For example, colocalization of EBER-positive and CD20$^+$/CD30$^+$ blasts with CD3$^+$ and PD-1$^+$ cells was observed in a case of renal infiltration (Figure 9, A and B) and in a different case in which a similar constellation was present in liver tissue (Figure 9C). Quantification of EBER$^+$ cells in perivascular regions of the spleen showed a trend toward increased levels of EBER detection in mice developing macroscopically detectable tumors, although results were variable (Figure 10, A and C, and Supplemental Figure S2). In sum, histopathology analysis complemented the analysis of homogenized tissues (analyzed by fluorescence-activated cell sorting) by clarifying the spatial distribution of infiltrating immune cells and by enabling spatially resolved subtyping (Figure 10, B and D).

Discussion

In a previous study, Lee et al[19] showed that the immune cell composition in long-term humanized mice played an important role in the development and shaping of EBV-induced B-cell lymphoma. EBV-associated HL was seen exclusively in mice after long-term (15-week) human reconstitution and particularly on coimplantation of mesenchymal stem cells expressing a Delta like non-canonical notch ligand 1 (DLK1), resulting in human CD3$^+$ T-cell skewing. In this study, infections with EBV strains derived from the B95.8 virus and engineered to coexpress reporter genes were performed at 15 to 17 weeks after huHSCT. Therefore, T cells were allowed to resume development and to be activated naturally by the EBV infection and/or resulting tumorigenesis. Furthermore, in this study, CD8$^+$ and CD4$^+$ T-cell expansion was sequentially monitored in blood by longitudinal flow cytometry analyses, showing CD8$^+$ T lymphocytes vigorously expanding because of infection and particularly because of tumor development. In several lymphatic tissues, especially when tumor growth was observed (eg, spleen, lymph nodes), this resulted in a massive accrual in the absolute CD8$^+$ T-cell numbers. Nevertheless, this enormous increase in the numbers of CTLs was unable to counteract tumor growth and may even support tumor development. This assumption was backed by high PD-1 expression on partially dysfunctional CD8$^+$ T cells and also detection of a Tim-3$^+$PD1$^+$ severely dysfunctional population, raising the possibility of blunted or even tumor-promoting immune responses. Histopathological analyses further highlighted that the PD-1$^+$ T-cell–rich infiltrates and early manifestations of perivascular tumor spread colocalized, further supporting the notion of inefficient immune cell–tumor cell interactions that do not result in tumor clearance. Thus, in our work, tumor occurrence and extreme T-cell activation patterns confirmed the previously observed findings,[19] but in contrast to Lee et al,[19] who concluded that these EBV-induced tumors resembled HL, this study provides evidence for a potential role of the extreme T-cell activation and dysfunctional CTL patterns codeveloping with a highly malignant lymphoproliferative disease, resembling monomorphic post-transplant lymphoproliferative disorder or high-grade diffuse-large B-cell lymphoma. These results rather go along with clinical findings obtained by Macedo et al[32] from the analyses of asymptomatic pediatric thoracic organ transplant patients with high EBV load carriers, showing increased frequencies of EBV-specific CD8$^+$ T cells with CD38, PD-1, and CD127 up-regulation, features of cellular exhaustion. These results pointed to the importance of chronic EBV load and of the levels of antigenic pressure in shaping EBV-specific memory CD8$^+$ T cells, underlining the potential relevance of immunologic monitoring of EBV-specific CD8$^+$ T cells in the clinic. Indeed, a separate clinical study by Bingler et al[33] analyzed asymptomatic patients who carried high EBV viral loads over prolonged periods and concluded that this chronic high EBV load state was a predictor of *de novo* or recurrent post-transplant lymphoproliferative disorder. Our combined results suggested that the brisk immunologic response in humanized mice could support tumor seeding in peripheral organs and promote early phases of local tumor lesions. Using humanized NOD/severe combined immune-deficient *IL2rg*^{null} mice engrafted with

human fetal bone marrow $CD34^+$ cells together with human thymus and liver (BLT model), other groups showed that the capacity of T cells to prevent EBV-related oncogenic transformation and to control growth of EBV-associated tumors, derived from *in vitro* infected B cells, was variable and could be modulated by therapeutic interventions.[17,18,34,35] In another type of model, monoclonal antibodies blocking the T-cell inhibitory receptors, PD-1 and cytotoxic T−lymphocyte-associated protein 4 (CTLA-4), enhanced the ability of adoptive T cells selected from cord blood to control the EBV infection and the outgrowth of $PD\text{-}L1^+/PD\text{-}L2^+$ lymphomas in mice challenged with cord blood B cells infected with EBV *in vitro*.[36] The main overall issue with these previous models is that the T-cell reconstitution was weak and/or provided adoptively, not allowing the human leukocyte antigen−restricted immune editing process (ie, by which the immune-suppressive TME could restrict productive antitumor immune responses). Furthermore, the analyses of the human immune reconstitution were expanded to several lymphatic tissues (ie, including BM, mLN, and LN), and systemic effects could be assessed. This may be important in mouse models testing new immune therapies to foresee organ-specific effects or toxicities. Another remarkable finding was the perivascular spread of $PD\text{-}1^+$ cells colocalizing with tumors. This is important from the clinical perspective, as the clinical effect can be potentially optimized if immune therapies could be delivered preferentially to highly vascularized tumor localizations. Furthermore, innovative developments in noninvasive imaging and computed tomographic analyses could in the future provide precise and dynamic spatiotemporal information regarding the immune potency of novel therapies to subvert oncogenesis. In summary, in this work, we extended the analyses of humanized mice infected with EBV toward a fully endogenous, persistent, and dynamic codevelopment of tumors and T cells, ultimately leading to immune exhaustion, whereby the tumors ultimately maintained the upper hand. In sum, this straightforward working model containing tumor and immune cells developing in mice from the same human subject reproduced clinical findings obtained in post-transplant patients and will be suitable to demonstrate preclinical proof of concept of novel immune therapies *in vivo*. A straightforward validation would be to examine if this CTL dysfunctional phenotype can be rescued with an antibody therapy directed toward PD-1 in humanized mice infected with EBV, as currently performed for tumor models.

Acknowledgments

We thank all members of the Regenerative Immune Therapies Applied Laboratory for valuable contributions.

R.S. planned the project, designed experiments, obtained funding and regulatory approvals, enrolled collaborators, interpreted the data, wrote the second draft, and edited the final manuscript; S.D. and C.S. conducted experiments, analyzed data, performed the statistical analyses, and wrote the first manuscript draft; F.F. performed the histopathological analyses, generated figures, and edited the final manuscript; N.K. established and performed histopathological staining and *in situ* hybridization; B.E.-V. assisted in the setup and conducted the ELISpot assays; M.A., R.Z., T.T., Y.-F.A.C., and W.H. generated and produced the genetically modified Epstein-Barr virus strains and edited the final manuscript; A.S., S.J.T., and A.C. assisted in preparation and analyses of humanized mice; S.L. and A.B. assisted with technical know-how for the computed tomographic analyses; C.v.K. procured cord blood for generation of the humanized mice.

Supplemental Data

Supplemental material for this article can be found at *https://doi.org/10.1016/j.ajpath.2018.11.014*.

References

1. Yarchoan M, Hopkins A, Jaffee EM: Tumor mutational burden and response rate to PD-1 inhibition. N Engl J Med 2017, 377:2500−2501
2. Ansell SM, Lesokhin AM, Borrello I, Halwani A, Scott EC, Gutierrez M, Schuster SJ, Millenson MM, Cattry D, Freeman GJ, Rodig SJ, Chapuy B, Ligon AH, Zhu L, Grosso JF, Kim SY, Timmerman JM, Shipp MA, Armand P: PD-1 blockade with nivolumab in relapsed or refractory Hodgkin's lymphoma. N Engl J Med 2015, 372:311−319
3. Walsh NC, Kenney LL, Jangalwe S, Aryee KE, Greiner DL, Brehm MA, Shultz LD: Humanized mouse models of clinical disease. Annu Rev Pathol 2017, 12:187−215
4. Audige A, Rochat MA, Li D, Ivic S, Fahrny A, Muller CKS, Gers-Huber G, Myburgh R, Bredl S, Schlaepfer E, Scherrer AU, Kuster SP, Speck RF: Long-term leukocyte reconstitution in NSG mice transplanted with human cord blood hematopoietic stem and progenitor cells. BMC Immunol 2017, 18:28
5. Pearson T, Shultz LD, Miller D, King M, Laning J, Fodor W, Cuthbert A, Burzenski L, Gott B, Lyons B, Foreman O, Rossini AA, Greiner DL: Non-obese diabetic-recombination activating gene-1 (NOD-Rag1 null) interleukin (IL)-2 receptor common gamma chain (IL2r gamma null) null mice: a radioresistant model for human lymphohaematopoietic engraftment. Clin Exp Immunol 2008, 154:270−284
6. Sundarasetty B, Volk V, Theobald SJ, Rittinghausen S, Schaudien D, Neuhaus V, Figueiredo C, Schneider A, Gerasch L, Mucci A, Moritz T, von Kaisenberg C, Spineli LM, Sewald K, Braun A, Weigt H, Ganser A, Stripecke R: Human effector memory T helper cells engage with mouse macrophages and cause graft-versus-host-like pathology in skin of humanized mice used in a nonclinical immunization study. Am J Pathol 2017, 187:1380−1398
7. Lang J, Kelly M, Freed BM, McCarter MD, Kedl RM, Torres RM, Pelanda R: Studies of lymphocyte reconstitution in a humanized mouse model reveal a requirement of T cells for human B cell maturation. J Immunol 2013, 190:2090−2101
8. Harris DT, Badowski M: Long term human reconstitution and immune aging in NOD-Rag (-)-gamma chain (-) mice. Immunobiology 2014, 219:131−137
9. Hidalgo M, Amant F, Biankin AV, Budinska E, Byrne AT, Caldas C, Clarke RB, de Jong S, Jonkers J, Maelandsmo GM, Roman-Roman S, Seoane J, Trusolino L, Villanueva A: Patient-derived xenograft models: an emerging platform for translational cancer research. Cancer Discov 2014, 4:998−1013
10. Wang M, Yao LC, Cheng M, Cai D, Martinek J, Pan CX, Shi W, Ma AH, De Vere White RW, Airhart S, Liu ET, Banchereau J,

Brehm MA, Greiner DL, Shultz LD, Palucka K, Keck JG: Humanized mice in studying efficacy and mechanisms of PD-1-targeted cancer immunotherapy. FASEB J 2018, 32:1537−1549
11. Kutok JL, Wang F: Spectrum of Epstein-Barr virus-associated diseases. Annu Rev Pathol 2006, 1:375−404
12. Islas-Ohlmayer M, Padgett-Thomas A, Domiati-Saad R, Melkus MW, Cravens PD, Martin Mdel P, Netto G, Garcia JV: Experimental infection of NOD/SCID mice reconstituted with human CD34+ cells with Epstein-Barr virus. J Virol 2004, 78:13891−13900
13. Shultz LD, Saito Y, Najima Y, Tanaka S, Ochi T, Tomizawa M, Doi T, Sone A, Suzuki N, Fujiwara H, Yasukawa M, Ishikawa F: Generation of functional human T-cell subsets with HLA-restricted immune responses in HLA class I expressing NOD/SCID/IL2r gamma(null) humanized mice. Proc Natl Acad Sci U S A 2010, 107:13022−13027
14. Fujiwara S, Imadome K, Takei M: Modeling EBV infection and pathogenesis in new-generation humanized mice. Exp Mol Med 2015, 47:e135
15. Traggiai E, Chicha L, Mazzucchelli L, Bronz L, Piffaretti JC, Lanzavecchia A, Manz MG: Development of a human adaptive immune system in cord blood cell-transplanted mice. Science 2004, 304: 104−107
16. Melkus MW, Estes JD, Padgett-Thomas A, Gatlin J, Denton PW, Othieno FA, Wege AK, Haase AT, Garcia JV: Humanized mice mount specific adaptive and innate immune responses to EBV and TSST-1. Nat Med 2006, 12:1316−1322
17. Strowig T, Gurer C, Ploss A, Liu YF, Arrey F, Sashihara J, Koo G, Rice CM, Young JW, Chadburn A, Cohen JI, Munz C: Priming of protective T cell responses against virus-induced tumors in mice with human immune system components. J Exp Med 2009, 206: 1423−1434
18. Ma SD, Hegde S, Young KH, Sullivan R, Rajesh D, Zhou Y, Jankowska-Gan E, Burlingham WJ, Sun X, Gulley ML, Tang W, Gumperz JE, Kenney SC: A new model of Epstein-Barr virus infection reveals an important role for early lytic viral protein expression in the development of lymphomas. J Virol 2011, 85:165−177
19. Lee EK, Joo EH, Song KA, Choi B, Kim M, Kim SH, Kim SJ, Kang MS: Effects of lymphocyte profile on development of EBV-induced lymphoma subtypes in humanized mice. Proc Natl Acad Sci U S A 2015, 112:13081−13086
20. Baer R, Bankier AT, Biggin MD, Deininger PL, Farrell PJ, Gibson TJ, Hatfull G, Hudson GS, Satchwell SC, Seguin C, Tuffnell PS, Barrell BG: DNA sequence and expression of the B95-8 Epstein-Barr virus genome. Nature 1984, 310:207−211
21. Palser AL, Grayson NE, White RE, Corton C, Correia S, Ba Abdullah MM, Watson SJ, Cotten M, Arrand JR, Murray PG, Allday MJ, Rickinson AB, Young LS, Farrell PJ, Kellam P: Genome diversity of Epstein-Barr virus from multiple tumor types and normal infection. J Virol 2015, 89:5222−5237
22. Delecluse HJ, Hilsendegen T, Pich D, Zeidler R, Hammerschmidt W: Propagation and recovery of intact, infectious Epstein-Barr virus from prokaryotic to human cells. Proc Natl Acad Sci U S A 1998, 95: 8245−8250
23. Warming S, Costantino N, Court DL, Jenkins NA, Copeland NG: Simple and highly efficient BAC recombineering using galK selection. Nucleic Acids Res 2005, 33:e36
24. Skorupski K, Taylor RK: Positive selection vectors for allelic exchange. Gene 1996, 169:47−52
25. Wang S, Zhao Y, Leiby M, Zhu J: A new positive/negative selection scheme for precise BAC recombineering. Mol Biotechnol 2009, 42: 110−116
26. Steinbruck L, Gustems M, Medele S, Schulz TF, Lutter D, Hammerschmidt W: K1 and K15 of Kaposi's sarcoma-associated herpesvirus are partial functional homologues of latent membrane protein 2A of Epstein-Barr virus. J Virol 2015, 89: 7248−7261
27. Volk V, Reppas AI, Robert PA, Spineli LM, Sundarasetty BS, Theobald SJ, Schneider A, Gerasch L, Deves Roth C, Kloss S, Koehl U, von Kaisenberg C, Figueiredo C, Hatzikirou H, Meyer-Hermann M, Stripecke R: Multidimensional analysis integrating human T-cell signatures in lymphatic tissues with sex of humanized mice for prediction of responses after dendritic cell immunization. Front Immunol 2017, 8:1709
28. Salguero G, Daenthanasanmak A, Munz C, Raykova A, Guzman CA, Riese P, Figueiredo C, Langer F, Schneider A, Macke L, Sundarasetty BS, Witte T, Ganser A, Stripecke R: Dendritic cell-mediated immune humanization of mice: implications for allogeneic and xenogeneic stem cell transplantation. J Immunol 2014, 192:4636−4647
29. Sukdolak C, Tischer S, Dieks D, Figueiredo C, Goudeva L, Heuft HG, Verboom M, Immenschuh S, Heim A, Borchers S, Mischak-Weissinger E, Blasczyk R, Maecker-Kolhoff B, Eiz-Vesper B: CMV-, EBV- and ADV-specific T cell immunity: screening and monitoring of potential third-party donors to improve post-transplantation outcome. Biol Blood Marrow Transplant 2013, 19:1480−1492
30. Singer M, Wang C, Cong L, Marjanovic ND, Kowalczyk MS, Zhang H, Nyman J, Sakuishi K, Kurtulus S, Gennert D, Xia J, Kwon JYH, Nevin J, Herbst RH, Yanai I, Rozenblatt-Rosen O, Kuchroo VK, Regev A, Anderson AC: A distinct gene module for dysfunction uncoupled from activation in tumor-infiltrating T cells. Cell 2016, 166:1500−15011.e9
31. Cibrian D, Sanchez-Madrid F: CD69: from activation marker to metabolic gatekeeper. Eur J Immunol 2017, 47:946−953
32. Macedo C, Webber SA, Donnenberg AD, Popescu I, Hua Y, Green M, Rowe D, Smith L, Brooks MM, Metes D: EBV-specific CD8+ T cells from asymptomatic pediatric thoracic transplant patients carrying chronic high EBV loads display contrasting features: activated phenotype and exhausted function. J Immunol 2011, 186:5854−5862
33. Bingler MA, Feingold B, Miller SA, Quivers E, Michaels MG, Green M, Wadowsky RM, Rowe DT, Webber SA: Chronic high Epstein-Barr viral load state and risk for late-onset posttransplant lymphoproliferative disease/lymphoma in children. Am J Transplant 2008, 8:442−445
34. Ma SD, Yu X, Mertz JE, Gumperz JE, Reinheim E, Zhou Y, Tang W, Burlingham WJ, Gulley ML, Kenney SC: An Epstein-Barr virus (EBV) mutant with enhanced BZLF1 expression causes lymphomas with abortive lytic EBV infection in a humanized mouse model. J Virol 2012, 86:7976−7987
35. Yajima M, Imadome K, Nakagawa A, Watanabe S, Terashima K, Nakamura H, Ito M, Shimizu N, Yamamoto N, Fujiwara S: T cell-mediated control of Epstein-Barr virus infection in humanized mice. J Infect Dis 2009, 200:1611−1615
36. Ma SD, Xu X, Jones R, Delecluse HJ, Zumwalde NA, Sharma A, Gumperz JE, Kenney SC: PD-1/CTLA-4 blockade inhibits Epstein-Barr virus-induced lymphoma growth in a cord blood humanized-mouse model. PLoS Pathog 2016, 12:e1005642